International Journal of Nanomedicine

Dovepress
Taylor & Francis Group

Open Access Full Text Article

ORIGINAL RESEARCH

Antimicrobial and Anti-Biofilm Activity of Dichlorophen-Functionalized Gold Nanoparticles Against Carbapenem-Resistant *Enterobacteriaceae*

Panjie Hu[1,2], Huale Chen[1,2], Changrui Qian[1,2], Qingxia Fu[1,2], Shihang Zhang[1,2], Zeyu Huang[1,2], Haifeng Liu[1,2], Cui Zhou[1,2], Mo Shen[1,2], Tieli Zhou[1,2]

[1]Department of Clinical Laboratory, The First Affiliated Hospital of Wenzhou Medical University, Wenzhou, Zhejiang, People's Republic of China; [2]Key Laboratory of Clinical Laboratory Diagnosis and Translational Research of Zhejiang Province, Wenzhou, Zhejiang, People's Republic of China

Correspondence: Mo Shen; Tieli Zhou, Department of Clinical Laboratory, The First Affiliated Hospital of Wenzhou Medical University, Wenzhou, Zhejiang, People's Republic of China, Email shenmo601@163.com; wyztli@163.com

Purpose: The global emergence and spread of carbapenem-resistant *Enterobacteriaceae* (CRE) represent a major threat to effective clinical antimicrobial therapy, highlighting the urgent demand for alternative treatment strategies. This study aims to develop dichlorophen-functionalized gold nanoparticles (DDM_Au NPs) as a novel approach to combat CRE and their associated biofilms.

Methods: Two structurally related antiparasitic compounds, bithionol and dichlorophen, were functionalized with Au NPs using a one-pot synthesis technique and thoroughly characterized. Their antibacterial activity was assessed through standard antimicrobial susceptibility testing and bacterial growth curve analysis. Antibiofilm properties were evaluated using crystal violet staining, scanning electron microscopy, and confocal laser scanning microscopy. The underlying mechanism of action was investigated by measuring reactive oxygen species production and assessing bacterial membrane permeability. Biocompatibility was evaluated via hemolysis assays, in vivo murine studies, and *Galleria mellonella* infection models. A urinary catheter model contaminated with biofilms, along with murine models of abdominal and pulmonary infection, was employed to assess device-associated applicability and therapeutic efficacy in vivo.

Results: DDM_Au NPs demonstrated potent antibacterial activity against CRE, with minimum inhibitory concentrations ranging from 4 to 16 μg/mL. These nanoparticles effectively inhibited biofilm formation and promoted the disruption of mature biofilms, resulting in bacterial load reductions of 2–6 $\log_{10}$ CFU/mL on infected urinary catheters. Mechanistic studies revealed that their antimicrobial activity was primarily driven by disruption of bacterial membrane integrity and induction of intracellular oxidative stress through elevated reactive oxygen species production. Notably, DDM_Au NPs exhibited favorable biocompatibility and significantly reduced bacterial burdens at infection sites by 4–5 $\log_{10}$ CFU/mL, while also alleviating inflammatory responses and limiting tissue damage across multiple animal infection models.

Conclusion: This study introduces a streamlined and effective strategy for achieving both antibacterial and antibiofilm effects using antiparasitic drug-functionalized Au NPs. DDM_Au NPs show strong promise as innovative antimicrobial agents for treating clinical CRE infections and reducing environmental contamination in healthcare environments.

Keywords: anti-biofilm, antiparasitic drug, carbapenem-resistant *Enterobacteriaceae*, dichlorophen, gold nanoparticle

Introduction

The global rise in antibiotic-resistant bacteria has led to a significant increase in infections and mortality, posing a serious threat to public health and placing a considerable economic burden on healthcare systems worldwide.[1] The misuse and overuse of carbapenems—often considered the "last line" of defense against multidrug-resistant gram-negative pathogens—have contributed to the emergence of carbapenem-resistant strains. In its 2025 Global Priority Pathogen List, the World Health Organization identified carbapenem-resistant *Enterobacteriaceae* (CRE) as a critical priority pathogen group, underscoring the urgent need for novel antibiotics.[2] Biofilm formation further complicates the issue of bacterial

Received: 4 June 2025
Accepted: 13 August 2025
Published: 25 August 2025

Graphical Abstract

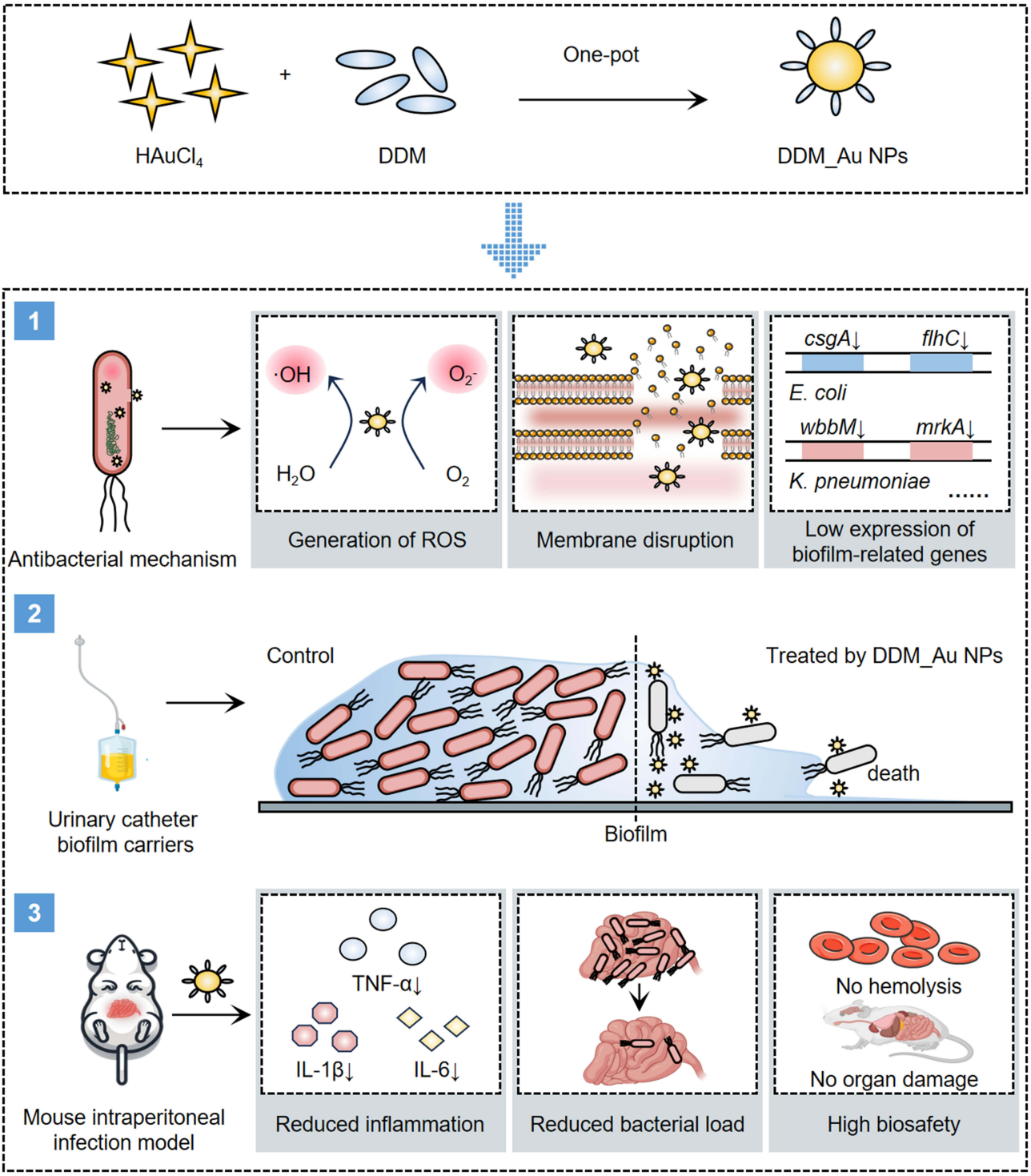

resistance, as it enhances bacterial survival and tolerance to antibiotics. CRE strains readily form biofilms, facilitating colonization of patients and contamination of hospital environments. This capability significantly contributes to hospital-acquired infections and has been linked to major outbreaks in healthcare facilities.[3] Such infections include ventilator-associated pneumonia, abdominal infections, and catheter-associated urinary tract and bloodstream infections.[4] To

combat severe infections caused by CRE, researchers have increasingly focused on developing new antibiotics or chemically modifying existing ones. However, the pace of antimicrobial drug discovery and production continues to lag behind the rapid evolution of resistance, with high development costs and significant failure risks further impeding progress.[5] In this context, nanomaterials with intrinsic antimicrobial properties have emerged as a promising alternative strategy to address the antibiotic resistance crisis.

Nanotechnology has gained widespread application across multiple biomedical fields, including infection management, targeted drug delivery, and cancer therapy.[6] Elemental metals such as silver, gold, copper, and iron exhibit broad-spectrum antimicrobial effects when engineered at the nanoscale.[7] Among them, gold nanoparticles (Au NPs) are especially attractive due to their unique physicochemical properties, including chemical inertness, biocompatibility, excellent stability, and high functionalization potential.[8] Despite their advantages, earlier Au NP-based antimicrobial approaches have faced challenges such as limited stability, dose-dependent cytotoxicity, suboptimal delivery efficiency, and poor in vivo efficacy. For instance, unmodified Au NPs demonstrate only weak intrinsic antibacterial activity (effective dose ~197 μg/mL), and the high concentrations required to achieve therapeutic effects can induce toxicity, including oxidative stress and damage to the liver, kidneys, and nervous system.[9] Surface functionalization of Au NPs can substantially lower the required dose, thereby reducing associated toxicities.[10] While cationic Au NPs can effectively interact with bacterial membranes, they often exert cytotoxic effects by disrupting host cell membranes due to electrostatic interactions with negatively charged phospholipid bilayers. In contrast, drug-functionalized Au NPs with anionic surfaces typically display improved biocompatibility and enhanced safety profiles.[11] However, prolonged storage of Au NPs at ambient temperatures may compromise their stability by increasing particle size and reducing zeta potential, thereby diminishing antibacterial activity.[12] Notably, antibiotics conjugated to Au NPs have been shown to outperform their free-drug counterparts by enhancing delivery, cellular uptake, and site-specific targeting.[13] Nevertheless, many Au NP-based formulations still require high doses (~10 mg/kg) to achieve therapeutic outcomes in murine infection models, a concentration much higher than those effective in vitro, reflecting their limited translational efficacy.[14,15] To overcome these limitations, diverse strategies have been employed to functionalize Au NPs with antimicrobial agents. Gold cores modified with clinically approved antibiotics, plant extracts, bacteriophage ligands, aminophenol derivatives, and even sweeteners have demonstrated enhanced antibacterial performance.[8,14,16–18] These modifications aim to improve therapeutic efficacy while minimizing cytotoxicity and overcoming challenges associated with stability and delivery.

Phenolic compounds have excellent reducing capacity and chemical stability, making them suitable modifiers for Au NPs to impart antimicrobial properties.[19] In our previous study, we demonstrated the antimicrobial activity of bithionol (BT).[20] BT and dichlorophen dimethyl ether (DDM) are structurally similar antiparasitic agents, both containing multiple hydroxyl groups, which make them suitable candidates for modifying Au NPs for antibacterial applications. BT is a clinically approved antiparasitic agent used in the treatment of schistosomiasis and has shown antimicrobial activity against certain gram-positive bacteria. However, its efficacy against gram-negative bacteria remains limited.[20] DDM, a US Food and Drug Administration (FDA)-approved drug for treating intestinal tapeworm infections, similarly exhibits antibacterial activity predominantly against gram-positive organisms. In contrast, it shows poor and narrow-spectrum activity against gram-negative bacteria such as *Escherichia coli*.[21,22] Importantly, dermal toxicity studies have indicated that DDM, when applied at concentrations up to 10% on rabbit skin, causes minimal or no irritation, suggesting that it does not act as a sensitizer.[23] Nanostructuring of antiparasitic drugs offers a promising strategy to enhance their activity against gram-negative bacteria by increasing drug loading capacity, improving delivery efficiency, and exploiting the multifaceted antimicrobial mechanisms of Au NPs. Despite this potential, the nanomodification of antiparasitic drugs for targeting gram-negative pathogens such as CRE has not yet been reported.

In this study, we utilized BT and DDM as functionalizing agents to synthesize drug-functionalized Au NPs, which were then evaluated for their antibacterial activities against CRE. Our findings revealed that dichlorophen-functionalized Au NPs (DDM_Au NPs) exhibited smaller particle sizes, superior antibacterial activity, and improved biocompatibility compared with bithionol-functionalized Au NPs (BT_Au NPs). DDM_Au NPs effectively treated CRE infections and eliminated CRE biofilm contamination in catheter models. Mechanistic investigations indicated that the antimicrobial action was primarily mediated through disruption of the bacterial cell membrane and induction of intracellular reactive

oxygen species (ROS) production. This novel approach, integrating antiparasitic drugs with nanomaterials, may provide a new therapeutic avenue for the treatment of CRE infections.

Materials and Methods

Bacterial Strains

In this study, 15 strains were obtained from the First Affiliated Hospital of Wenzhou Medical University (Zhejiang, China). The standard strains used included *Escherichia coli (E. coli)* ATCC 25922 and *Klebsiella quasipneumoniae* ATCC 700603 (the National Clinical Laboratory Center). All strains were subjected to matrix-assisted laser desorption/ionization time-of-flight mass spectrometry (MALDI-TOF MS), performed in Lyon (France). This study was approved by the Ethics Committee for Clinical Research at the First Affiliated Hospital of Wenzhou Medical University (Approval No. KY2025-R150). Considering the retrospective design of the study, the requirement for informed consent was waived.

Preparation and Characterization of Au NPs

The preparation of drug-modified Au NPs was based on a previously reported one-pot method, with appropriate modifications.[14] Briefly, hydrogen tetrachloroaurate was simultaneously mixed with a reducing and a stabilizing agent in a single step to yield organic or inorganic Au NPs.[14] For the preparation of DDM_Au NPs, sterile ddH_2O (10 mL) was mixed with triethylamine (50 μL), Tween 80 (150 mg), and DDM (0.1 mmol). This mixture was sonicated for 15 min. Simultaneously, $HAuCl_4 \cdot 3H_2O$ (0.05 mmol, 200 μL) was added to the mixture drop-wise on a magnetic agitator at 500 rpm. The resulting solution was continuously stirred for 2 h, during which its appearance changed from colorless to purple-red.[24] For the preparation of BT_Au NPs, sterile ddH_2O (10 mL) was mixed with triethylamine (50 μL), Tween 80 (50 mg), and BT (0.05 mmol). The resulting mixture was sonicated for 15 min, to which hydrogen tetrachloroaurate-(III) ($HAuCl_4 \cdot 3H_2O$) (0.05 mmol, 200 μL) was added drop-wise on a magnetic agitator at 1000 rpm at 20°C. The solution was then continuously stirred for 2 h, during which its appearance changed from colorless to brown. The reduction method using sodium borohydride ($NaBH_4$; China National Pharmaceutical Group Chemical Reagent Co., Ltd., Shanghai, China) was employed to prepare pure Au NPs.[25]

The synthesized Au NPs were dialyzed (7000 Da Molecular Weight Cut-Off) to remove impurities and sterilized by filtration through a 0.22-μm sieve.[18] Nanoparticle size and dispersion were assessed using dynamic light scattering (DLS) with a Zetasizer Nano ZS90 analyzer (Malvern PANalytical, Worcestershire, UK) at 25°C, and each measurement was performed in triplicate.[15] Ultraviolet-visible (UV-vis) absorption spectra (400–700 nm, 1-nm interval) were assessed using a multifunctional enzyme labeler (BioTek Synergy NEO_2; Santa Clara, CA, USA). Transmission Electron Microscope-Energy Dispersive Spectroscopy (TEM-EDS) (JEOL JEMF200; Tokyo, Japan) was performed to characterize the morphologies and elemental composition ratio of nanomaterials through energy spectrum scanning. Fourier-transformed infrared spectroscopy (FTIR) (Nicolet iS20, Thermo Scientific, Waltham, MA, USA) was employed to characterize the functional groups of DDM_Au NPs. Briefly, the Attenuated Total Reflection accessory was placed in the spectrometer's optical path under dry conditions, and the air background was recorded. One drop of the sample was then applied onto the crystal surface, and the spectra were collected at a resolution of 4 cm^{-1} with 32 scans over the 400–4000 cm^{-1} wavenumber range.[14] For the nanoparticle stability analysis, the dialyzed DDM_Au NPs were stored at 4°C and tested after 7 days, 9 months, and 18 months for their respective DLS profiles and UV–vis absorption spectra.[12]

Drug Sensitivity Test

According to the Clinical and Laboratory Standards Institute (CLSI) guidelines published in 2023, antibiotic sensitivity experiments were conducted to determine the minimum inhibitory concentrations (MICs) of the experimental strains to commonly used carbapenem antibacterial drugs, such as imipenem (IPM), meropenem (MEM), and ertapenem (ETP). The antibacterial activities of BT, DDM, Au NPs, BT_Au NPs, and DDM_Au NPs against the experimental strains were then determined.[26] The concentrations of BT/DDM used in this study corresponded to the content of BT/DDM present in the respective concentrations of BT_Au NPs/DDM_Au NPs and were dissolved in the same solvent used for the

synthesis of Au NPs. Next, 100 μL of the bacterial solution (1.5×10^6 CFU/mL) was added to each well of a 96-well plate containing 100 μL gradient concentration of the test drug, and the plate was incubated at 37°C for 16–18 h, followed by determination of the MIC values by visually assessing the extent of bacterial growth.

Red Blood Cell Hemolysis Test

This test was performed as described elsewhere.[27] Briefly, a 5% red blood cell suspension was prepared in PBS. Experimental treatments comprised varying concentrations of BT_Au NPs and DDM_Au NPs. PBS was used as the negative control, whereas 0.1% Triton X-100 (Beijing Solarbio Science and Technology Co., Ltd., China) was added to the suspension as a positive control. Both groups were co-cultured with 5% red blood cells at 37°C for 2 h, followed by centrifugation at 4°C at 13000 rpm for 5 min. Subsequently, the supernatant was transferred into a 96-well plate, and the absorbance was measured at 545 nm with an enzyme label. The hemolysis rate (%) was calculated using the following formula: Hemolysis rate (%) = $(OD_{\text{experimental group}} - OD_{\text{negative control group}})/(OD_{\text{positive control group}} - OD_{\text{negative control}})$, where OD is the optical density.

Growth Curve Test

The experiment was performed in accordance with previously described methods. MEM, a clinically used carbapenem, served as the antimicrobial drug control. LB medium was used to dilute overnight-cultured bacteria to a concentration of 1.5×10^6 CFU/mL.[28] Subsequently, 8 μg/mL of DDM_Au NPs, Au NPs, MEM (carbapenems are commonly used as drug controls), and the corresponding concentration of DDM were added, with PBS serving as the negative control. The absorbance value at 600 nm was measured at 0, 2, 4, 6, 12, and 24-h intervals, and a growth curve was constructed based on the obtained results.

Inhibition of Biofilm Formation

The experimental procedure was slightly modified, as outlined in the reference.[26] The staining method with crystal violet (CV; Beijing Solarbio Science and Technology Co., Ltd.) involved the addition of 100 μL of PBS (as a blank-control), MEM, DDM, Au NPs, and DDM_Au NPs to a 96-well plate. Subsequently, 100 μL of a fresh bacterial solution diluted with LB broth to a concentration of 1.5×10^6 CFU/mL was added to each well, and the plate was incubated at 37°C for 24 h. The wells were then washed twice with PBS, dried at room temperature, and stained with 1% CV for 10 min. After staining, CV was removed, and the wells were washed with PBS and allowed to dry. Then, an ethanol-acetone solution (95:5 v/v) was added to the wells, and the plate was incubated for 10 min, followed by reading of the absorbance value at 595 nm using an microplate reader. To determine the viable biofilm bacterial count, a similar procedure was employed.[29] Specifically, a 24-well plate was treated with 100 μL of the drug and 100 μL of the bacterial solution, and the plate was incubated at 37°C for 24 h. The medium was then gently removed, the plate was washed twice with PBS to eliminate the unadhered bacteria, and 200 μL of PBS was added to each well. Finally, ultrasonic vibration was applied to the plate for 10 min. The bacterial suspension was serially diluted, plated on LB agar, and cultured for 16–18 h. The resulting colonies were then enumerated.

Mature Biofilm Clearance Experiment

The experimental method was slightly modified, as described earlier.[26] The CV staining method was as follows: 200 μL of the fresh bacterial culture diluted with LB broth to 1.5×10^6 CFU/mL was added to the wells of a 96-well plate and incubated at 37°C for 48 h to obtain mature biofilms. The bacterial suspension was discarded and gently rinsed with PBS to remove the unadhered bacteria. After adding 200 μL of PBS (blank-control), MEM, DDM, Au NPs, and DDM_Au NPs at the corresponding concentrations, the plate was incubated at 37°C for 24 h. Cleaning, staining, and reading were then performed as previously mentioned.

The counting method for biofilm viable bacteria was performed as follows: first, a mature biofilm treated with different drugs (same as in the CV staining method) was obtained, and the medium in the 24-well plate was gently removed. The plates were washed with PBS twice, 200 μL of sterile PBS was added to each well, and ultrasonic

vibration was performed for 10 min. The obtained bacterial suspension was serially diluted ten times, coated on an agar plate, and cultured. Subsequently, the number of colonies was enumerated.[29]

Scanning Electron Microscopy (SEM)

Sterile square silicon wafers (5 × 5 mm) were put into wells, to which the bacterial solution and the corresponding drug (PBS or 1/2 MIC of DDM_Au NPs) were added. After incubation, the wafers were washed to remove the unadhered bacteria. Next, the samples were fixed in the dark at 4°C for 4 h with 2.5% (v/v) glutaraldehyde. The samples were then treated stepwise with a graded series of ethanol for 10 min each, followed by SEM imaging.[18]

Confocal Laser Scanning Microscopy

Six-well plates were filled with 500 μL of PBS, MEM, DDM, Au NPs, and DDM_Au NPs. Then, 500 μL of the bacterial solution (1.5×10^6 CFU/mL) was added. The plates were covered with aseptic cover slides and incubated at 37°C for 24 h to observe biofilm growth.[18] Liquid was gently removed, and 0.5 μM of SYTO 9 (Thermo Fisher Scientific (China) Co., Ltd., USA) and 0.3 μM of Propidium iodide (PI; Beijing Solarbio Sciences and Technology Co., Ltd.) were added. The samples were then examined under a confocal microscope (Nikon A1R-SIM-Storm; Tokyo, Japan) at a 60X magnification. The excitation wavelengths of 488 nm (green) and 561 nm (red), and emission wavelengths of 530 nm (green) and 617 nm (red) were used. Quantification of SYTO 9/PI fluorescence intensity was performed using ImageJ (National Institutes of Health) to determine the proportion of live and dead cells.[30]

Checkerboard Assay

For this assay, 50 μL of DDM was dispensed along the X-axis of a 96-well plate, creating a gradient dilution, which yielded a final concentration range of 256 to 0 μg/mL. Similarly, 50 μL of Au NPs was dispensed with a gradient dilution along the Y-axis, which yielded final concentrations ranging from 256 to 0 μg/mL. Subsequently, 100 μL of the bacterial suspension with a concentration of 1.5×10^6 CFU/mL was added. The plate was then incubated at 37°C for 16–18 h. The results were analyzed using the following formula: $FICI = (MIC_{DDM\ combined}/MIC_{DDM\ alone}) + (MIC_{Au\ NPs\ combined}/MIC_{Au\ NPs\ alone})$.

ROS Detection Assay/Clearance Assay

Bacteria were cultured overnight and diluted to obtain an OD_{600} of 0.3–0.4, incubated with the fluorescent probe in the dark at 37°C for 20 min. The free probe was removed, incubated with PBS, or DDM, Au NPs, and DDM_Au NPs at 37°C for 1 h. The fluorescence values (λ_{Exc}: 488 nm, λ_{Em}: 535 nm) were then measured.[19] For the ROS clearance experiments, gradient concentrations of diluted DDM_Au NPs (50 μL) were added to a 96-well clearance plate, followed by the addition of 50 μL of the ROS clearance agent, quercetin (MedChemexpress Biotechnology company, USA), to obtain a final concentration of 16 μg/mL.[18] Subsequently, 100 μL of the bacterial suspension (1.5×10^6 CFU/mL) was added to each well and the plate was incubated at 37°C for 16–18 h.

Membrane Permeability Test

Bacteria in the logarithmic growth phase, at an OD_{600} of 0.3–0.4, were exposed to different concentrations of PBS (blank-control), DDM, Au NPs, or DDM_ Au NPs for 2 h.[15] Subsequently, the bacteria were treated with either 50 μg/mL of PI or 30 μM of NPN solution for 30 min. Fluorescence intensity was measured with excitation/emission wavelengths of 535/615 nm for PI and 350/420 nm for NPN.

Urinary Catheter Biofilm Contamination Model

Sterile catheters were sliced into 1-cm segments and incubated in a bacterial suspension (1.5×10^6 CFU/mL) at 37°C for 48 h to allow biofilm formation. After gentle washing to remove planktonic bacteria, the catheter segments were transferred into fresh media containing DDM (8–16 μg/mL), Au NPs, DDM_Au NPs, or PBS, and further incubated at 37°C for 16–18 h. After gently washing the catheter, it was transferred into 1 mL of PBS for 10 min and provided with

ultrasonic shock to elute and disperse the biofilm. The number of viable bacteria present in the biofilm on the catheter was calculated by the colony counting method.[31]

Quantitative Reverse Transcription-Polymerase Chain Reaction (RT-qPCR)

The experimental strains in the logarithmic growth stage were adjusted to an OD_{600} of 0.6−0.8 with fresh broth. Equal amounts of PBS (blank-control group), DDM, Au NPs, and DDM_Au NPs (1/2 MIC) were added and allowed to oscillate at 180 rpm for 6 h. Total mRNA was extracted by using the Trizol method, followed by RT using an RT kit (Applied Biosystems, Waltham, MA, USA). The obtained cDNA was quantified by using a SYBR Green kit (Applied Biosystems) to analyze the expression of biofilm-related genes. The data were normalized to those of 16S rRNA for comparison. The primers used in the study were derived from the existing literature and have been listed in Table S1.[32,33]

In vivo Safety Assessment of Animals

The in vivo safety profile of DDM_Au NPs was assessed through intraperitoneal injection in mice and via an injection in *Galleria mellonella* larvae. The animals were randomly assigned to groups with reference to a random number table. All outcome measurements were performed by an independent investigator unaware of the grouping system. Quantitative data were obtained using automated analyzers to ensure objectivity. Humane endpoints were established following institutional guidelines, including rapid body weight loss of >20%, anorexia, and severe weakness impairing the ability to eat or drink independently.

The mouse experiments in this study were conducted using the Institute of Cancer Research (ICR) mice (male, age: 6–8 weeks, weight: 25 ±2 g; specific pathogen-free [SPF]; Charles River, Hangzhou, China) maintained under standard conditions in accordance with the Chinese National Laboratory Animal Standards (GB14925−2010). The mouse experiments were approved by the Ethics Committee of the First Affiliated Hospital of Wenzhou Medical University (Approval No. SYXK 2021–0017) and were conducted in accordance with the Wenzhou Laboratory Animal Welfare and Ethics Guidelines. A total of 30 mice were randomly assigned to the following five groups of 6 biological replicates each: PBS (blank-control) group and DDM_Au NPs groups treated with four different concentrations (2.5, 5, 7.5, and 10 mg/kg).[34] Intraperitoneal injections were administered every 12 h for 7 days, and the body weight was recorded. After collecting blood samples from the eye socket, the mice were euthanized, and their lungs, heart, spleen, and kidneys were collected. Blood samples were analyzed using a fully automated blood cell analyzer (Mindray BC-2800vet; Shenzhen, China) for the complete blood count (n = 3 biological replicates per group), and a fully automated biochemical analyzer (Chemray 240; Rayto, Shenzhen, China) for the serum levels of alanine aminotransferase (ALT), aspartate aminotransferase (AST), blood urea nitrogen (BUN), and creatinine (CREA) (n = 3 biological replicates/group). Tissue pathology sections were prepared by slicing the organs, which were then stained with hematoxylin and eosin (H&E). Inflammatory cell infiltration was observed under a microscope. Each group included at least three biological replicates (n = 3 biological replicates/group), and the representative images are shown.

The selection criteria for *G. mellonella* larvae included the identification of final instar larvae (weight: 250–350 mg), as characterized by a uniformly creamy-yellow color without any dark markings and an even weight distribution, following established literature guidelines.[35] Similarly, the criteria for determining death relied on the absence of response to mechanical stimulation, as described previously. The larvae were randomly assigned into the following 6 groups of 10 biological replicates each: PBS group and DDM_Au NPs groups treated with 5 different concentrations (ie, 7 × 4, 7 × 8, 7 × 16, 7 × 32, and 7 × 64 μg/mL, adjusted for a 7-fold dilution considering larval body fluid). Each larva received a 10-μL injection of sterile PBS into the left foot of the second-to-last pair of feet via a microinjector and allowed to stand for 2 h. Subsequently, a 10 μL volume of the respective drug concentration was injected into the right foot, ensuring consistency with the in vivo infection model. Larval survival was monitored over 7 days.

In vivo Animal Infection Model

Considering the ethical permissibility, cost-effectiveness, and physiological similarities to mammals in terms of drug metabolism and immune responses, *G. mellonella* serves as a suitable model for evaluating antimicrobial efficacy and drug safety in vivo.[36] The *G. mellonella* in vivo infection model was prepared by using a fresh bacterial suspension in

logarithmic growth phase diluted to 1×10^8 CFU/mL. Larvae were randomly assigned to one of the following 5 groups of 10 biological replicates each: PBS (blank-control), MEM, DDM, Au NPs, and DDM_Au NPs. A 10 μL bacterial suspension was injected into the left foot of each larva via a microinjector for 2 h, followed by the injection of 10 μL of 7× MIC DDM_Au NPs and the corresponding drug concentrations into the right foot. The survival rates were monitored over 7 days.

In the mouse abdominal infection model, 20 mice were randomly assigned to the following 5 groups of 4 biological replicates each: PBS, MEM, DDM, Au NPs, and DDM_Au NPs. The mice were infected via an intraperitoneal injection of a 200 μL bacterial solution (DC8647, 5×10^7 CFU/mL) for 2 h, followed by the injection of either PBS or 2.5 mg/kg drug (selected to evaluate efficacy at a lower, safer dose, consistent with published dosing strategies).[37] Subsequently, the mice were euthanized, and their abdominal lavage fluid and blood samples were collected. Bacterial colonies were enumerated, and the inflammatory factor levels were measured by ELISA.[38] For the mouse lung infection model (n = 3 biological replicates/group), following anesthesia, each mouse received 25 μL of the bacterial suspension (FK6793, 2×10^9 CFU/mL) via tracheal instillation using a nebulizer and was infected for 2 h before administering 50 μL of the treatment (at approximately 2 mg/kg). After 24 h, the mice were euthanized, and the lung tissues were collected, homogenized for colony counting, and processed for histopathological analyses with H&E staining.[39]

Statistical Analysis

All experiments were performed in triplicate (n = 3), unless otherwise specified. Data were presented as the mean ± standard deviation (SD) from at least three independent experiments. Statistical significance was assessed using Student's *t*-test and one-way analysis of variance (ANOVA). Statistical analyses were performed with GraphPad Prism 9.0 software.

Results

Preparation and Characterization of Au NPs

Various functionalized Au NPs were rapidly synthesized using an environmentally friendly one-pot method. Both DDM and BT contain multiple phenolic hydroxyl groups, which serve as effective reducing agents for converting Au^{3+} ions into elemental gold (Au^0) in solution (Figure 1A). DLS analysis revealed that BT_Au NPs exhibited a single, narrow size distribution peak, with an average hydrodynamic diameter of 133.4 nm, a polydispersity index of 0.133, and a zeta potential of −29.33 mV. In contrast, DDM_Au NPs displayed a bimodal size profile, characterized by a minor peak at 1.85 nm and a dominant peak at 43.97 nm (polydispersity index = 0.578), along with a zeta potential of –22.35 mV (Figure 1B and C). UV–vis spectroscopy (Figure 1D) showed a well-defined surface plasmon resonance peak centered around 520 nm, confirming the formation of colloidal Au NPs. TEM images (Figure 1E) further supported these results, revealing aggregated "daisy-like" structures in BT_Au NPs, whereas DDM_Au NPs exhibited irregular morphologies. These findings are consistent with previously reported structural characteristics of Au NPs by Pathania et al.[40] The antibacterial potency of Au NPs is closely associated with their particle size, with those in the 1–100 nm range demonstrating enhanced antimicrobial and antibiofilm properties.[8] Of the two antiparasitic drug-functionalized Au NPs, DDM_Au NPs were more likely to fall within this optimal size window, which may partly explain their superior antimicrobial performance.

Coupled with the pronounced antibacterial activity observed in preliminary evaluations (see section "Antibacterial Activities of Different Formulations"), these findings supported the selection of DDM_Au NPs for further investigation. Comprehensive structural and chemical characterization was performed using TEM-EDS and FTIR. EDS mapping (Figure 2A) showed uniform elemental distribution of O, Cl, and Au within DDM_Au NPs, consistent with their morphology and supporting the successful synthesis of the nanomaterial. FTIR spectra (Figure 2B) revealed further evidence of DDM functionalization on the Au NP surface. Upon coordination with gold, characteristic features of Au NPs appeared in the fingerprint region. The broad O-H stretching band at 3378 cm^{-1} exhibited a notable red shift to 3180 cm^{-1}, likely due to enhanced hydrogen bonding arising from polar -OH groups introduced by DDM. Moreover, the intensity of the C=O stretching vibration at 1736 cm^{-1} was markedly reduced, and the appearance of a new

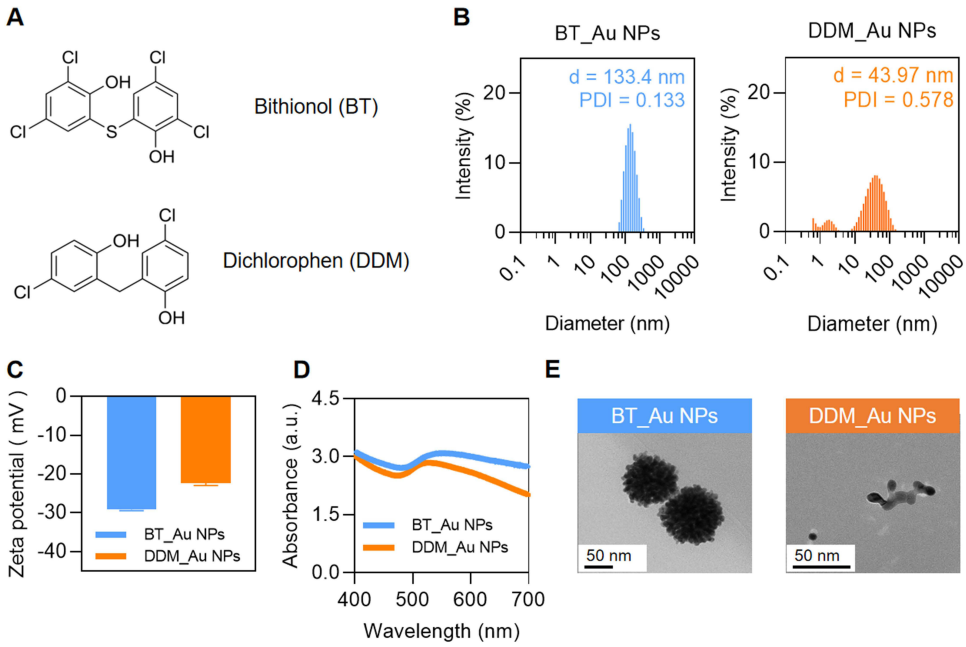

Figure 1 Characterizations of bithionol-decorated gold nanoparticles (BT_Au NPs) and dichlorophen-decorated gold nanoparticles (DDM_Au NPs). (**A**) Chemical structural formulas of BT and DDM; (**B**) Particle size and dispersion of BT_Au NPs and DDM_Au NPs; (**C**) Zeta potential of BT_Au NPs and DDM_Au NPs; (**D**) UV-Vis spectra of BT_Au NPs and DDM_Au NPs; (**E**) Transmission electron microscopic morphology of BT_Au NPs and DDM_Au NPs. PDI, polydispersity index; d, diameter.

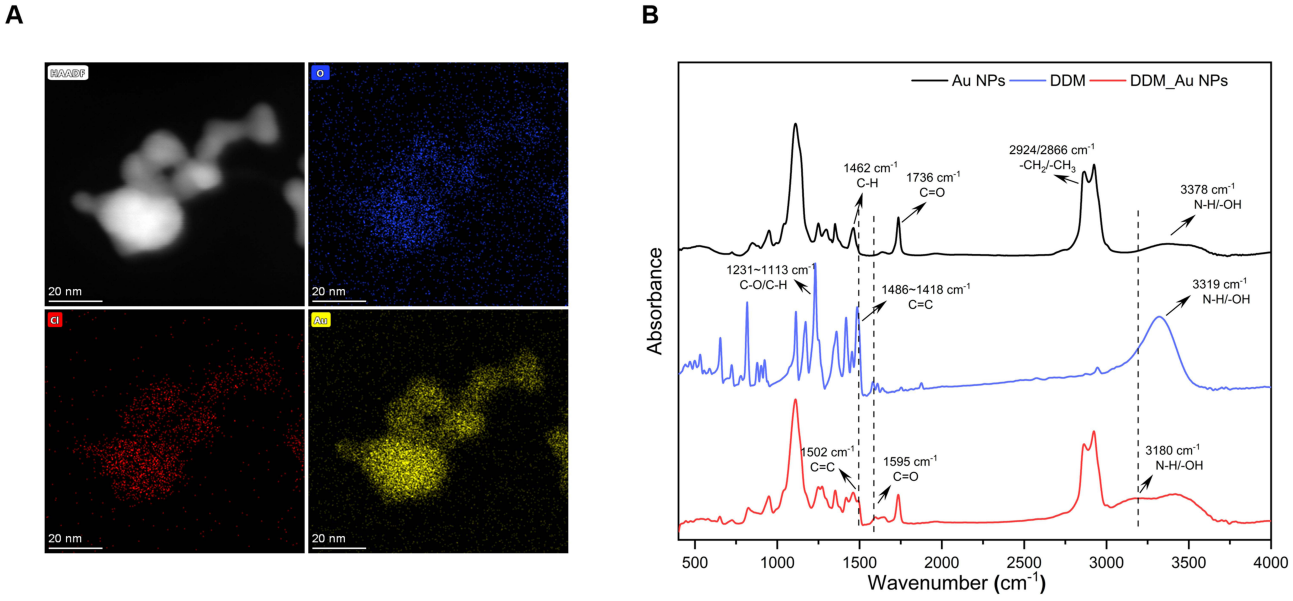

Figure 2 Further characterization of dichlorophen-decorated gold nanoparticles (DDM_Au NPs). (**A**) TEM mapping of DDM_Au NPs; (**B**) FTIR spectra of DDM, Au NPs, and DDM_Au NPs. HAADF, high-angle annular dark-field.

antisymmetric COO^- stretching band at 1595 cm^{-1} indicated the formation of a coordination complex between DDM and the Au surface. This interaction may result from the binding of chloroauric acid to the N-H groups of triethylamine, forming an intermediate ammonium salt that facilitates the generation of DDM_Au NPs. The presence of aromatic C=C stretching bands at 1502 and 1425 cm^{-1} further confirmed the integration of DDM's aromatic structure, while peak broadening suggested a densely packed ligand layer on the nanoparticle surface. Collectively, these results confirm the strong and stable complexation of DDM on the Au NP surface, with C=O likely playing a key role in anchoring the drug to the gold core.

https://doi.org/10.2147/IJN.S532807

Table 1 MICs of the BT, DDM, Au NPs, BT_Au NPs and DDM_Au NPs Against the Strains Used in This Study

Species	Strains	MIC (μg/mL)				
		BT	BT_Au NPs	DDM	DDM_Au NPs	Au NPs
Escherichia coli	DC5113	≥256	8	≥256	4	≥256
	DC8647	≥256	16	≥256	8	≥256
	DC10494	≥256	8	≥256	16	≥256
	DC10694	≥256	16	≥256	4	≥256
	DC11722	≥256	8	≥256	4	≥256
	ATCC25922	≥256	16	≥256	8	≥256
Klebsiella spp.	FK3006	≥256	16	≥256	8	≥256
	FK6709	≥256	16	≥256	8	≥256
	FK6793	≥256	8	≥256	16	≥256
	FK7112	≥256	16	≥256	8	≥256
	FK7513	≥256	8	≥256	8	≥256
	ATCC700603	≥256	16	≥256	16	≥256
Enterobacter cloacae	CG1249	≥256	8	≥256	4	≥256
	CG1330	≥256	8	≥256	4	≥256
	CG1381	≥256	8	≥256	4	≥256
	CG1778	≥256	8	≥256	8	≥256
	CG1813	≥256	8	≥256	4	≥256

Antibacterial Activities of Different Formulations

The bacterial strains used in this study met the criteria for CRE, primarily characterized by carbapenemase-mediated resistance (Table S2), as previously described.[41,42] The antibacterial activity of BT_Au NPs and DDM_Au NPs was evaluated against these CRE strains. BT, DDM, and Au NPs alone demonstrated minimal to no antibacterial effects and were therefore included as negative controls to rule out any intrinsic antimicrobial activity of the individual components.[18] BT_Au NPs exhibited MICs ranging from 8–32 μg/mL, while DDM_Au NPs showed lower MICs of 4–16 μg/mL, indicating superior potency (Table 1). In comparison, commonly used carbapenems such as MEM, IPM, and ETP showed a wide range of MICs (0.5–512 μg/mL) across CRE isolates, with many strains exhibiting high-level resistance (eg, MEM and ETP ≥64 μg/mL, IPM ≥32 μg/mL) (Table S2).[43] Erythrocyte hemolysis assays further demonstrated that DDM_Au NPs at 64 μg/mL caused no discernible hemolytic activity, whereas BT_Au NPs at the same concentration induced significant hemolysis (Figure S1). Based on their enhanced antimicrobial performance, optimal size profile, and minimal hemolytic toxicity, DDM_Au NPs were prioritized for further evaluation of their antibacterial and antibiofilm properties.

Stability of DDM_Au NPs

The storage stability of DDM_Au NPs was assessed, with a focus on preserving their antimicrobial efficacy.[12] After storage at 4°C for 7 days and 9 months, DDM_Au NPs retained activity against CRE (MIC = 8–16 μg/mL), with only a one-fold increase in MIC in a small number of strains (Figure S2A). UV–vis spectroscopy revealed red-shifted peaks with increased absorbance intensity, coupled with enlarged particle size and elevated zeta potential over time, suggestive of gradual aggregation—particularly evident after 18 months of storage (Figures S2B–D). Nevertheless, the overall antibacterial efficacy remained largely intact after 9 months of storage.

Antibacterial Activity of DDM_Au NPs Against Actively Growing Bacteria and Biofilm Formation

As shown in Figure 3, DDM_Au NPs completely inhibited bacterial growth during the first 12 h post-treatment, whereas bacteria in the MEM, DDM, and Au NPs groups resumed rapid growth within 4–6 h.[18] Strains FK3006 and FK6793

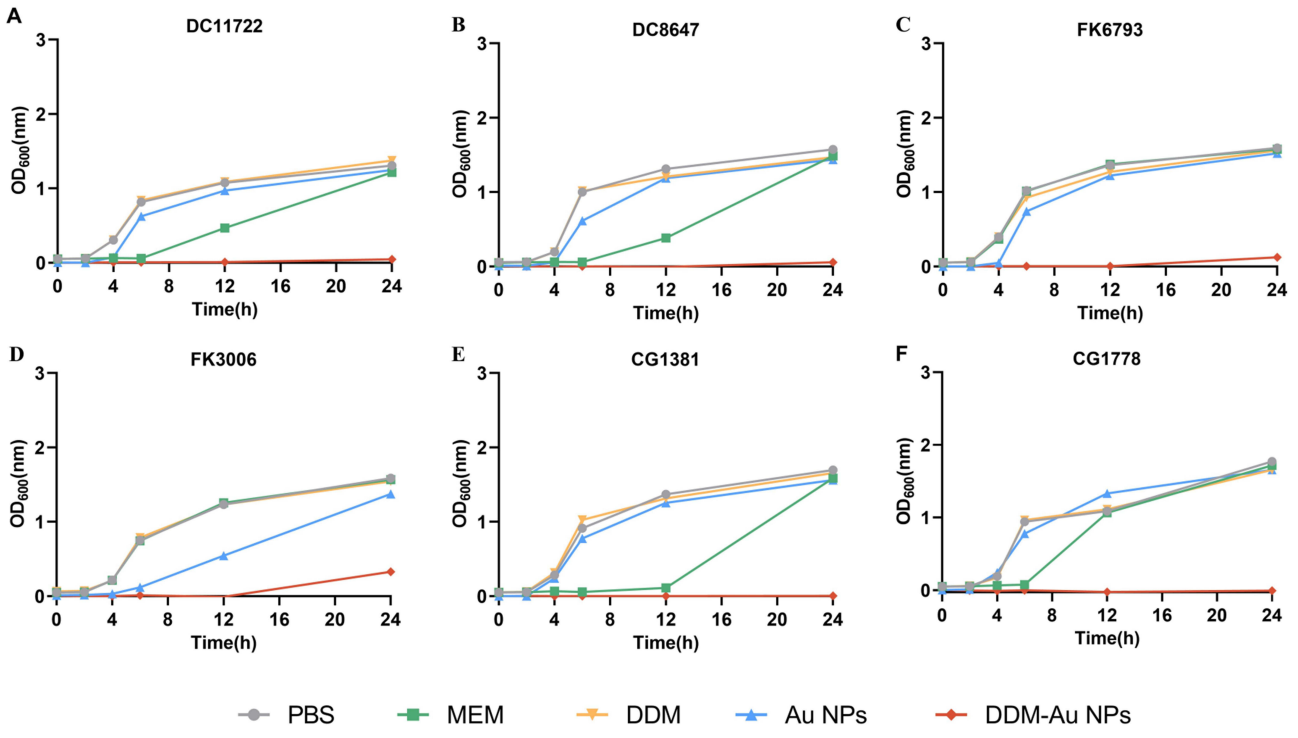

Figure 3 Growth curves of clinical CRE strains subjected to various treatments. (**A**) *E. coli* DC11722; (**B**) *E. coli* DC8647; (**C**) *K. pneumoniae* FK6793; (**D**) *K. pneumoniae* FK3006; (**E**) *E. cloacae* CG1381; (**F**) *E. cloacae* CG1778. Data are presented as the mean ±SD (n = 3).

showed regrowth after 12 h, indicating that repeated dosing or increased concentrations may be required for sustained suppression.[44]

Figure 4 illustrates the inhibitory effect of DDM_Au NPs on biofilm formation.[15] CV staining revealed a significant reduction in biofilm biomass following treatment with 1/4 and1/2 MIC concentrations of DDM_Au NPs compared with the untreated control (Figures 4A and B, $P < 0.05$). In parallel, viable cell counting demonstrated a significant decrease in the number of bacteria embedded within biofilms (Figure 4C, $P < 0.05$). The biofilm-eradicating potential of DDM_Au NPs was further confirmed (Figures 5A and B). Treatment with DDM_Au NPs at MIC and 2× MIC concentrations significantly reduced biofilm biomass compared with the control ($P < 0.05$). DDM_Au NPs effectively penetrated the dense extracellular matrix of the biofilm, eradicating embedded bacteria (Figure 5C). Notably, DDM_Au NPs exhibited substantially stronger antibiofilm activity and a greater reduction in viable bacterial counts than MEM ($P < 0.05$), offering a promising strategy to overcome the biofilm-associated tolerance that limits the efficacy of conventional antibiotics.

SEM further demonstrated the disruption of CRE biofilms upon treatment with DDM_Au NPs (Figure 6). At 3500× magnification, the biofilm appeared more porous and disorganized, with fewer intact bacterial cells. At 7000× magnification, treated bacteria showed signs of dispersion, morphological deformation, and cell rupture.[18] Confocal laser scanning microscopy using live/dead staining revealed intense red fluorescence and diminished green fluorescence in the DDM_Au NPs-treated group, indicating compromised membrane integrity and reduced viability of biofilm-associated bacteria (Figure S3A).[45] Quantitative analysis confirmed this, showing a marked drop in live cells (24.15%) compared to >92% viability in the PBS, DDM, and Au NPs groups (Figure S3B). These findings are consistent with colony counting results and confirm the robust antibiofilm efficacy of DDM_Au NPs.

Antibacterial Mechanism of DDM_Au NPs

Current studies suggest that DDM_Au NPs possess bactericidal and antibiofilm properties. To explore the potential mechanisms underlying their antibacterial effect, a series of experiments was conducted. A checkerboard drug sensitivity

https://doi.org/10.2147/IJN.S532807

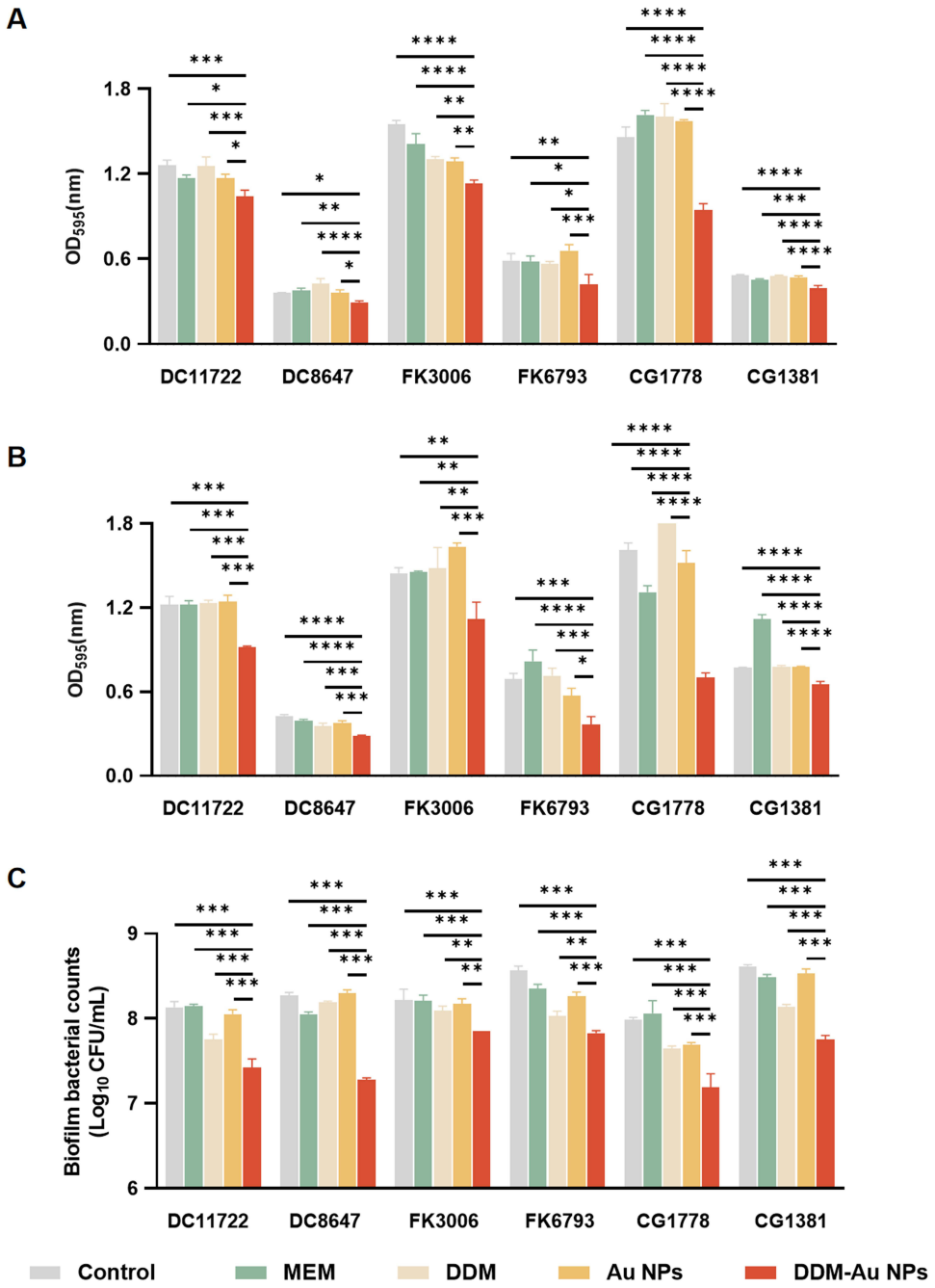

Figure 4 Ability of dichlorophen-decorated gold nanoparticles (DDM_Au NPs) to inhibit biofilm formation. (**A**) Crystal violet staining of biofilm formed after treatment with 1/4 MIC; (**B**) Crystal violet staining of biofilm formed after treatment with 1/2 MIC; (**C**) The viable bacteria count in the biofilm formed by CRE strains after treatment with 1/2 MIC of drugs; **P* < 0.05, ***P* < 0.01, ****P* < 0.001, *****P* < 0.0001. Data are presented as the mean ±SD (n = 3).

assay (Table S3) ruled out the possibility that the antibacterial activity resulted from a synergistic effect of DDM and Au NPs alone.[46] Quantitative assessment of intracellular ROS levels following different treatments (Figure 7A) revealed a significant increase in ROS in CRE strains after exposure to DDM_Au NPs ($P < 0.05$), with a clear concentration-dependent trend. To further examine this, an ROS scavenging assay was performed using quercetin, a known ROS inhibitor (Table S4).[47] Quercetin treatment led to a 4–16-fold or greater increase in the MIC of DDM_Au NPs, although some antibacterial efficacy persisted. It implies that oxidative stress contributes to, but is not solely responsible for, the bactericidal activity of DDM_Au NPs. These findings directed our focus to the impact of these nanomaterials on bacterial membrane permeability.

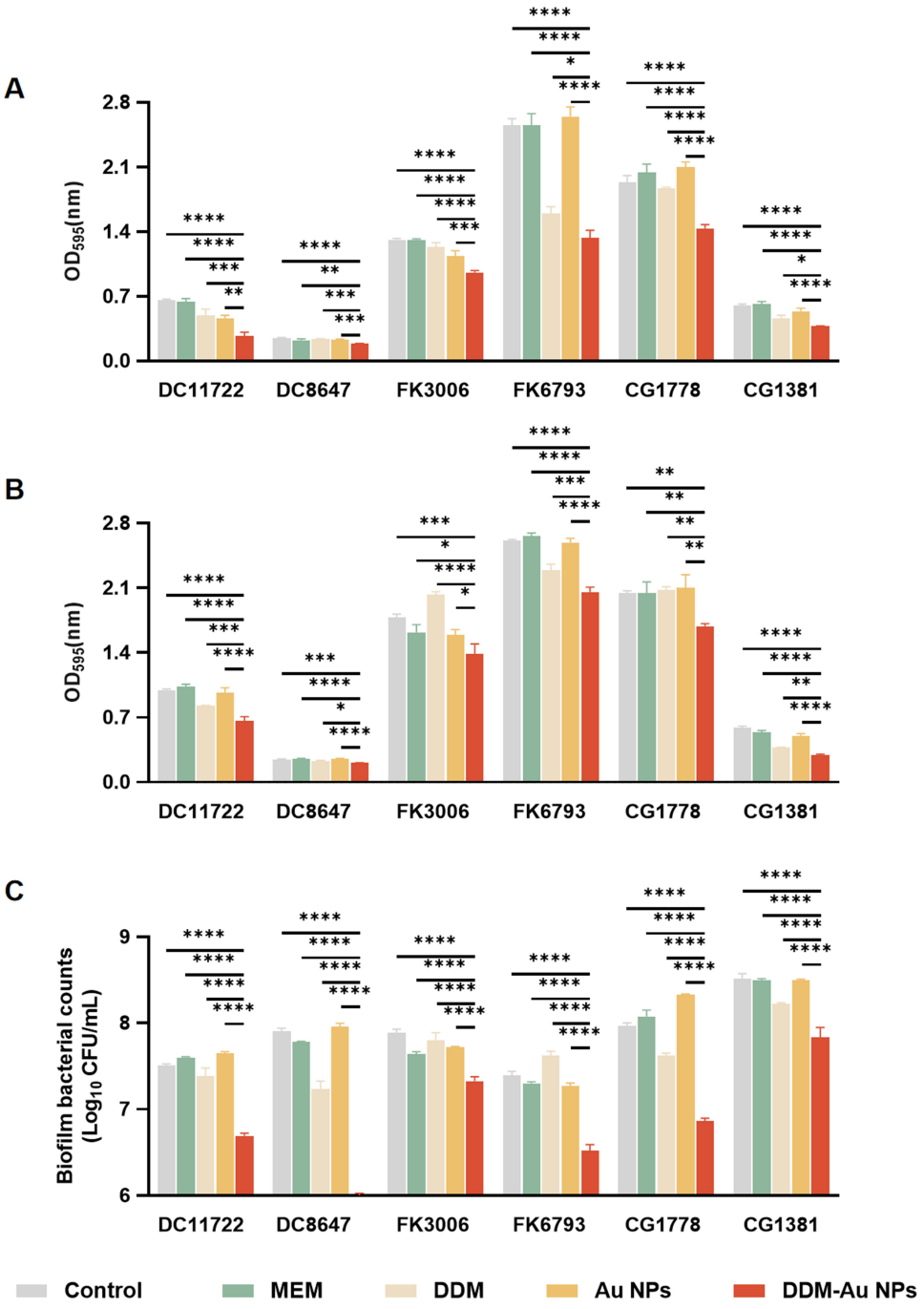

Figure 5 Ability of dichlorophen-decorated gold nanoparticles (DDM_Au NPs) to eliminate mature biofilms. (**A**) Crystal violet staining of mature biofilm of CRE strains after treatment with the MIC of drug; (**B**) Crystal violet staining of mature biofilm of CRE strains after treatment with 2× MIC of the drug; (**C**) The viable bacterial count in mature biofilm formed by CRE strains after treatment with the MIC of drugs; **P* < 0.05, ***P* < 0.01, ****P* < 0.001, *****P* < 0.0001. Data are presented as the mean ±SD (n = 3).

Experimental data shown in Figures 7B and C demonstrate that the fluorescence intensities of PI and NPN were significantly elevated in a dose-dependent manner following DDM_Au NPs treatment compared with the blank control group ($P < 0.05$). A similar trend was observed with DDM alone, particularly in relation to the outer membrane permeability. These findings confirmed that DDM_Au NPs disrupt bacterial membrane integrity, thereby impairing normal cellular functions.

https://doi.org/10.2147/IJN.S532807

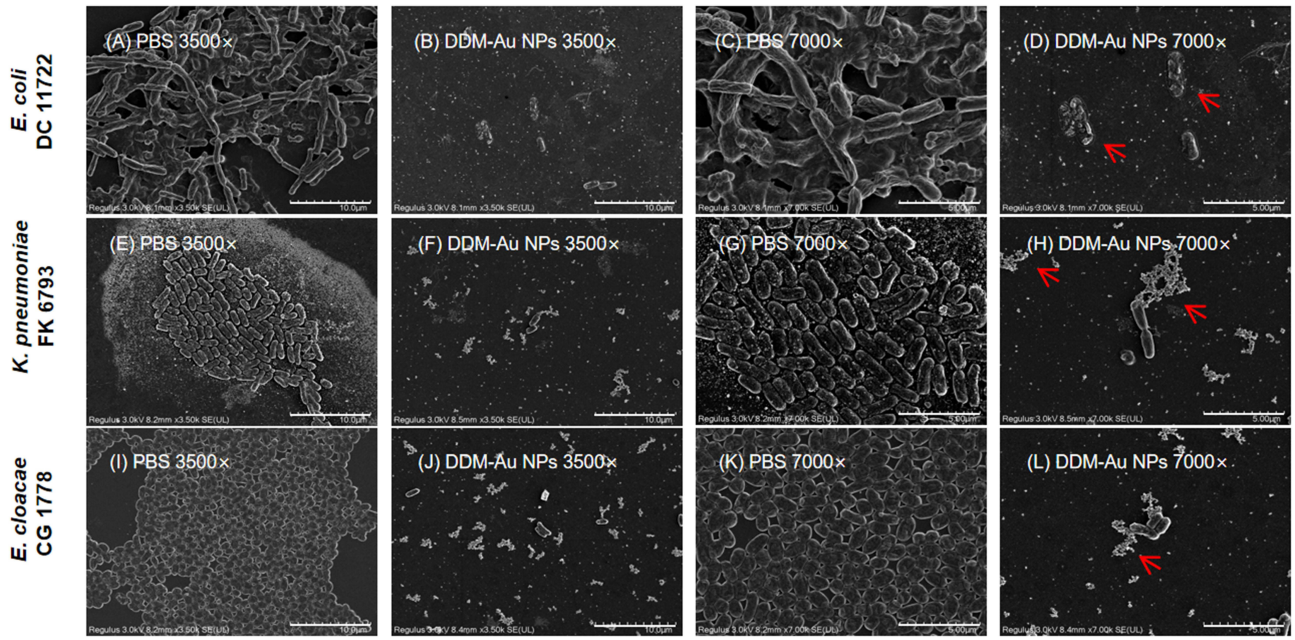

Figure 6 SEM image of biofilm formed by CRE strains treated with dichlorophen-decorated gold nanoparticles (DDM_Au NPs). (**A–D**) Biofilm formed by DC11722; (**E–H**) Biofilm formed by FK6793; (**I–L**) Biofilm formed by CG1778. The images are magnified at 3500× and 7000×; The red arrow indicates disrupted bacterial cells, leaked intracellular contents, and cellular debris.

Urinary Catheter Biofilm Infection Model

To evaluate the antibiofilm efficacy of DDM_Au NPs against CRE, a catheter biofilm contamination model was employed. Various strains were exposed to a standardized drug concentration to simulate clinical prophylactic use. Compared with the control, MEM, and individual DDM or Au NPs groups, the DDM_Au NPs group exhibited a marked reduction in viable bacteria on catheter-associated CRE biofilms across all tested strains ($P < 0.05$) (Figure 8). At 8 μg/mL, DDM_Au NPs decreased bacterial load by 6.40, 2.12, and 2.08 $\log_{10}$ CFU/mL in catheters infected with different CRE strains. At 16 μg/mL, reductions were 6.23, 3.53, and 2.87 $\log_{10}$ CFU/mL, respectively—most notably in carbapenem-resistant *E. coli*, highlighting the potential of DDM_Au NPs in preventing persistent urinary tract infections.

Biofilms are composed not only of bacterial cells but also of an extracellular matrix consisting primarily of water and polymeric substances like polysaccharides, forming a complex and protective microenvironment. Biofilm development is a regulated, dynamic process involving the expression of numerous critical genes.[48] Thus, we examined whether DDM_Au NPs influence the expression of biofilm-associated genes in CRE strains beyond their direct bactericidal effect.[33,49] As shown in Figure S4, RT-qPCR analysis revealed significant downregulation of biofilm-related genes—*csgA, csgD, flhC*, and *lsrB* in *E. coli*; and *wzm, wbbM, mrkA*, and *pgaA* in *Klebsiella pneumoniae* (*K. pneumoniae*)—following DDM_Au NPs treatment ($P < 0.05$). Notably, treatment with DDM alone also significantly suppressed the expression of these genes. These findings suggest that DDM_Au NPs inhibit biofilm formation by modulating the expression of biofilm-regulatory genes in CRE strains.

In vivo Application of DDM_Au NPs

The in vivo biosafety of DDM_Au NPs was evaluated in *G. mellonella* larvae and mice.[50] Following intravenous administration of DDM_Au NPs at doses of 2.5, 5, 7.5, and 10 mg/kg in mice, no mortality was observed across all groups (Figure 9A). Body weight remained stable throughout the treatment period (Figure 9B). Hematological profiles and serum biomarkers of hepatic and renal function showed no statistically significant differences compared with the PBS control group ($P > 0.05$) (Figure 9C and D). Histological examination of H&E-stained tissue sections from the heart, liver, spleen, lungs, and kidneys demonstrated preserved architecture without signs of hemorrhage, necrosis, inflammatory infiltration, or fibrosis (Figure 9E). In addition, exposure to DDM_Au NPs at concentrations ranging from 4 to

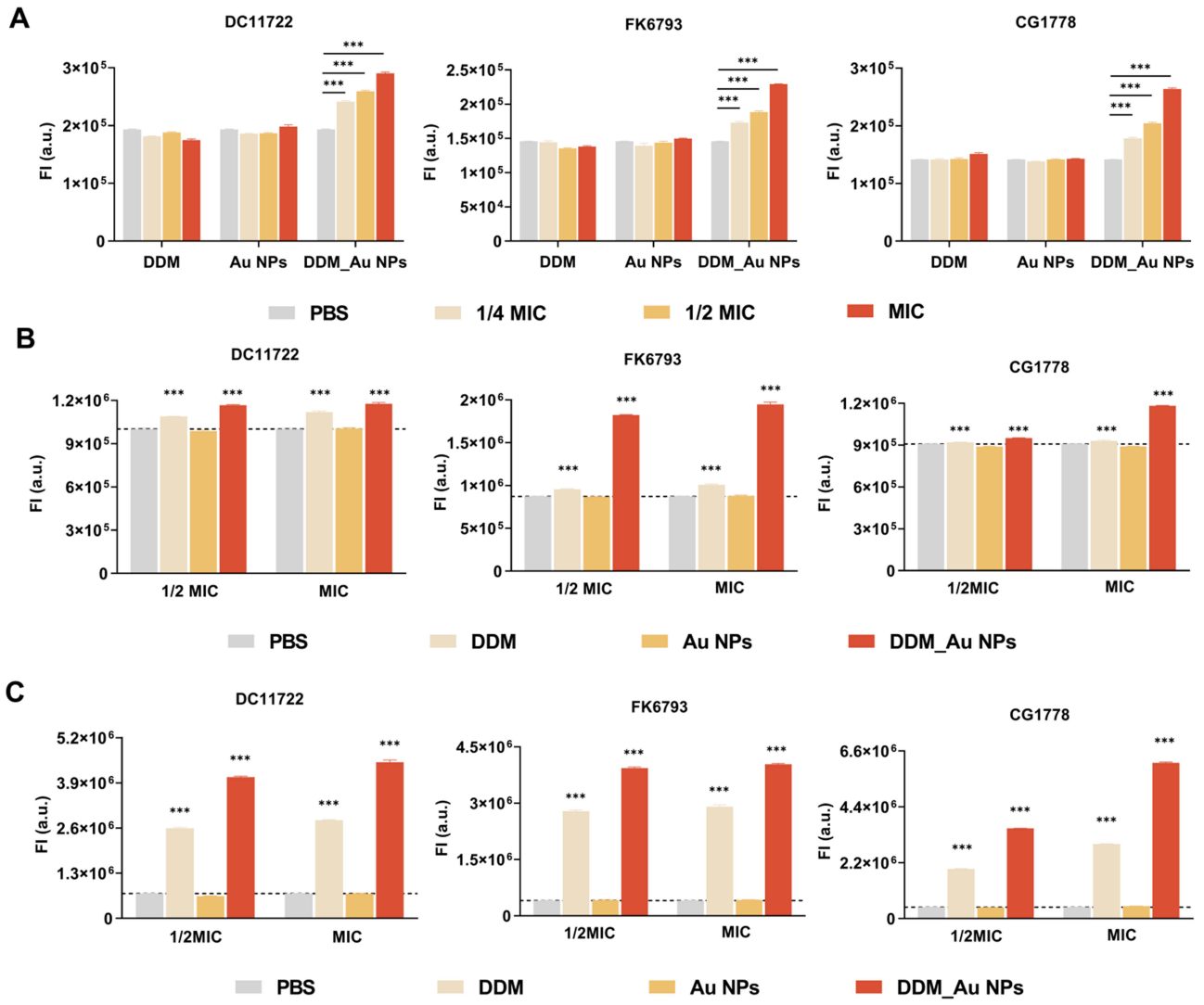

Figure 7 Mechanism of antibacterial action of dichlorophen-decorated gold nanoparticles (DDM_Au NPs). (**A**) Quantitative analysis of the ROS fluorescence levels; (**B**) Quantitative detection of the PI fluorescence values; (**C**) Quantitative detection of the NPN fluorescence values. Dotted line: average fluorescence value of the control group; ***$P < 0.001$. Data are presented as the mean ±SD (n = 3).

64 μg/mL did not induce significant toxicity in *G. mellonella* larvae (Figure S5A and B). Collectively, these findings provide preliminary evidence supporting the in vivo safety of DDM_Au NPs.[34] Given the absence of observable toxicity, subsequent in vivo therapeutic experiments were conducted.

To assess the therapeutic efficacy of DDM_Au NPs against CRE, a *G. mellonella* infection model was used to evaluate 7-day post-infection survival (Figure S5C). The DDM_Au NPs-treated group showed a significantly higher survival rate (60%) than the other groups (0–20%) ($P < 0.05$).

An acute peritoneal infection mouse model was developed to examine the impact of DDM_Au NPs on bacterial clearance and systemic inflammation (Figure 10A). Treatment with DDM_Au NPs significantly reduced bacterial counts in both the peritoneal cavity and bloodstream by more than 3 $\log_{10}$ CFU/mL (Figure 10B and C). Moreover, levels of proinflammatory cytokines—IL-1β, IL-6, and TNF-α—in the intraperitoneal lavage fluid and serum were significantly reduced in DDM_Au NPs-treated mice ($P < 0.05$) (Figure 10D and E). Given that *K. pneumoniae* is a prominent causative agent of hospital-acquired pneumonia globally, a murine acute lung infection model was employed to further assess the therapeutic potential of DDM_Au NPs (Figure 11A).[39] Mice infected with the FK6793 strain and treated with 2 mg/kg DDM_Au NPs exhibited a reduction in lung bacterial burden by at least 2 $\log_{10}$ CFU/mL compared with other

https://doi.org/10.2147/IJN.S532807

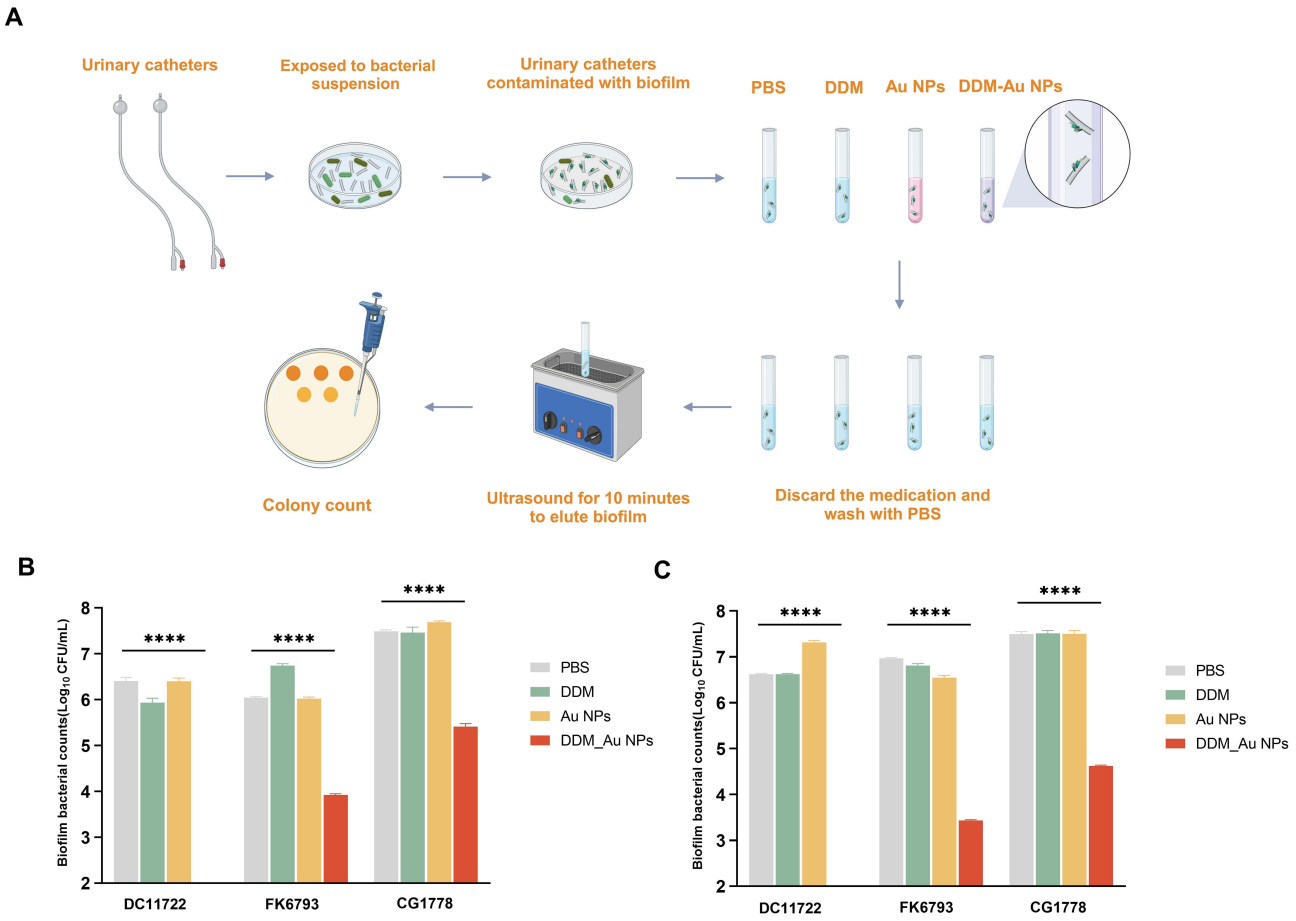

Figure 8 Urinary catheter biofilm contamination model. (**A**) Depiction of the experimental process; (**B**) The live bacterial count in the biofilm of urinary catheters contaminated with CRE strains after treatment with 8 μg/mL of DDM_Au NPs; (**C**) The live bacterial count in the biofilm of urinary catheters contaminated with CRE strains after treatment with 16 μg/mL of DDM_Au NPs. The absence of numerical groups in the figure represents values below the countable range (<2 Log_{10} CFU/mL); ****$P < 0.0001$. Data are presented as the mean ±SD (n = 3).

treatment groups (Figure 11B). Histopathological evaluation of lung tissues stained with H&E revealed that mice in the PBS, MEM, DDM, and Au NPs treatment groups showed extensive inflammatory cell infiltration, alveolar wall destruction, and varying degrees of edema, congestion, and hemorrhage. In contrast, lung tissues from DDM_Au NPs-treated mice displayed notably reduced inflammatory cell infiltration and only mild alveolar damage (Figure 11C). These results underscore the therapeutic promise of DDM_Au NPs in managing acute pulmonary infections.

Discussion

With the ongoing escalation of bacterial resistance, humanity is confronting the alarming threat of a post-antibiotic era. Projections indicate that by 2050, antimicrobial resistance (AMR) could result in up to 10 million deaths annually—surpassing current global cancer-related mortality.[51] This public health crisis is anticipated to cause economic losses exceeding $2 trillion by 2050, largely driven by the misuse and overuse of antibiotics.[1] In *Enterobacteriaceae*, carbapenem resistance may arise from carbapenemase production or non-carbapenemase β-lactamases in combination with reduced membrane permeability, rendering clinical treatments ineffective against CRE.[52] CRE infections are associated with exceptionally high crude mortality, with 30-day mortality rates reaching as high as 64% in patients with CRE-induced bloodstream infections.[53] In this study, we successfully demonstrated the feasibility of synthesizing Au NPs using antiparasitic drugs that possess multiple reducing groups, thereby broadening the therapeutic applications of these compounds in anti-infective treatment. Previous research has explored similar strategies wherein Au NPs were functionalized with agents such as plant extracts (eg, eugenol), artificial sweeteners (eg, aspartame), and synthetic

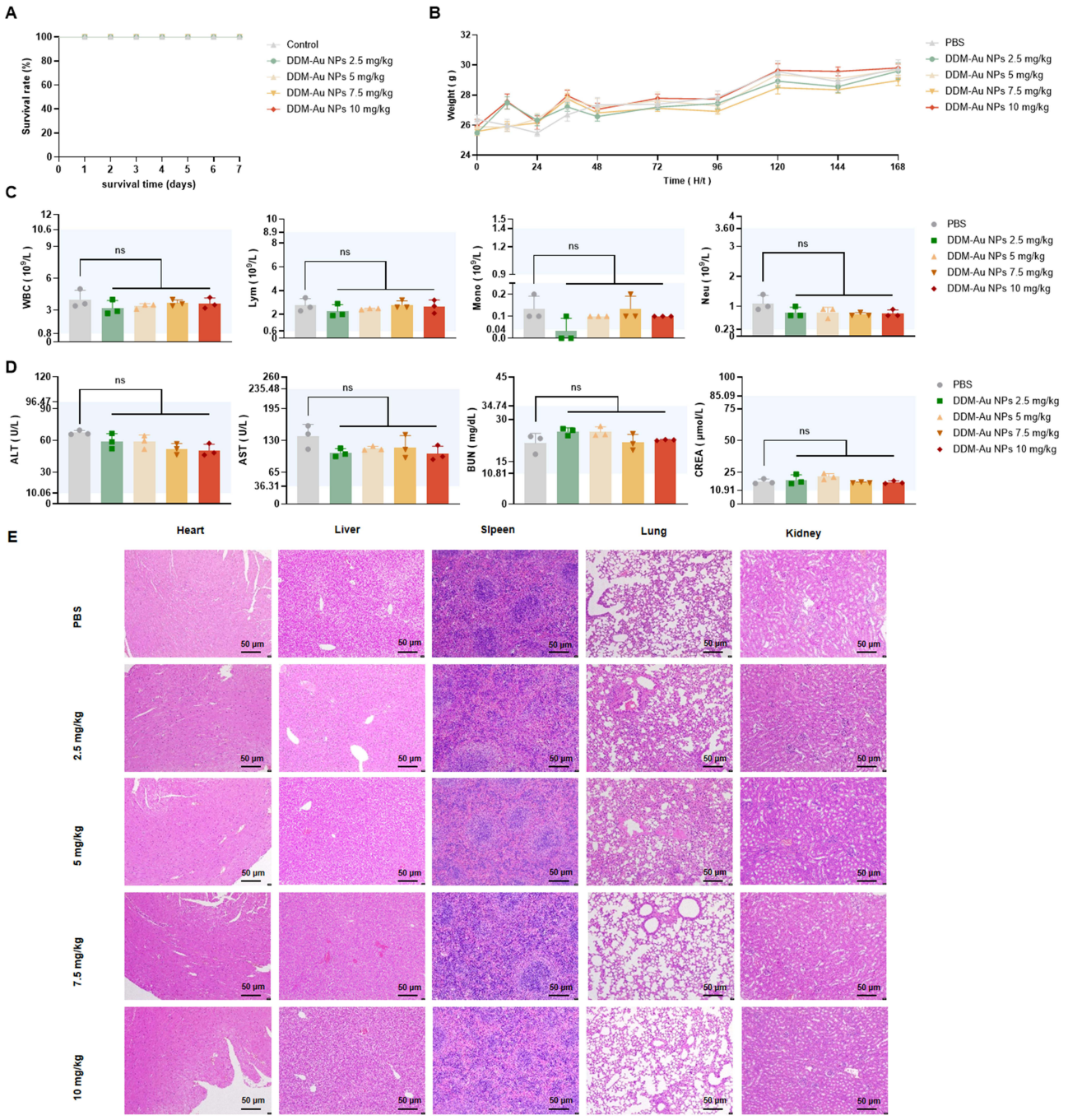

Figure 9 In vivo safety experiments in mice. (**A**) Seven-day survival curve of mice (n = 6); (**B**) Seven-day weight changes (n = 6); (**C**) Changes in the mouse blood routine (n = 3); (**D**) Changes in the serum liver and kidney function markers in mice (n = 3); (**E**) Representative H&E-stained histological sections of the major organs; The blue-shaded area represents the normal value range; $P > 0.05$ (ns). Data are presented as the mean ±SD.

chemicals (eg, aminophenol) to enhance antimicrobial efficacy.[14,18,25] Although Au NPs have previously been investigated as antimicrobial agents, our approach—leveraging antiparasitic drug-functionalized Au NPs to specifically target CRE—represents an innovative and promising therapeutic strategy.

Unlike other Au NPs modifiers such as eugenol (classified as a Group 2B carcinogen by the FDA),[54] aspartame (linked to possible neurotoxicity),[55] and para-aminophenol (associated with nephrotoxicity),[56] the antiparasitic drugs utilized in our study have already received FDA approval or clinical approval,[22] providing a strong foundation for the safety of these drug-based nanomaterials in potential clinical applications. Currently, FDA-approved nanotechnology-

https://doi.org/10.2147/IJN.S532807

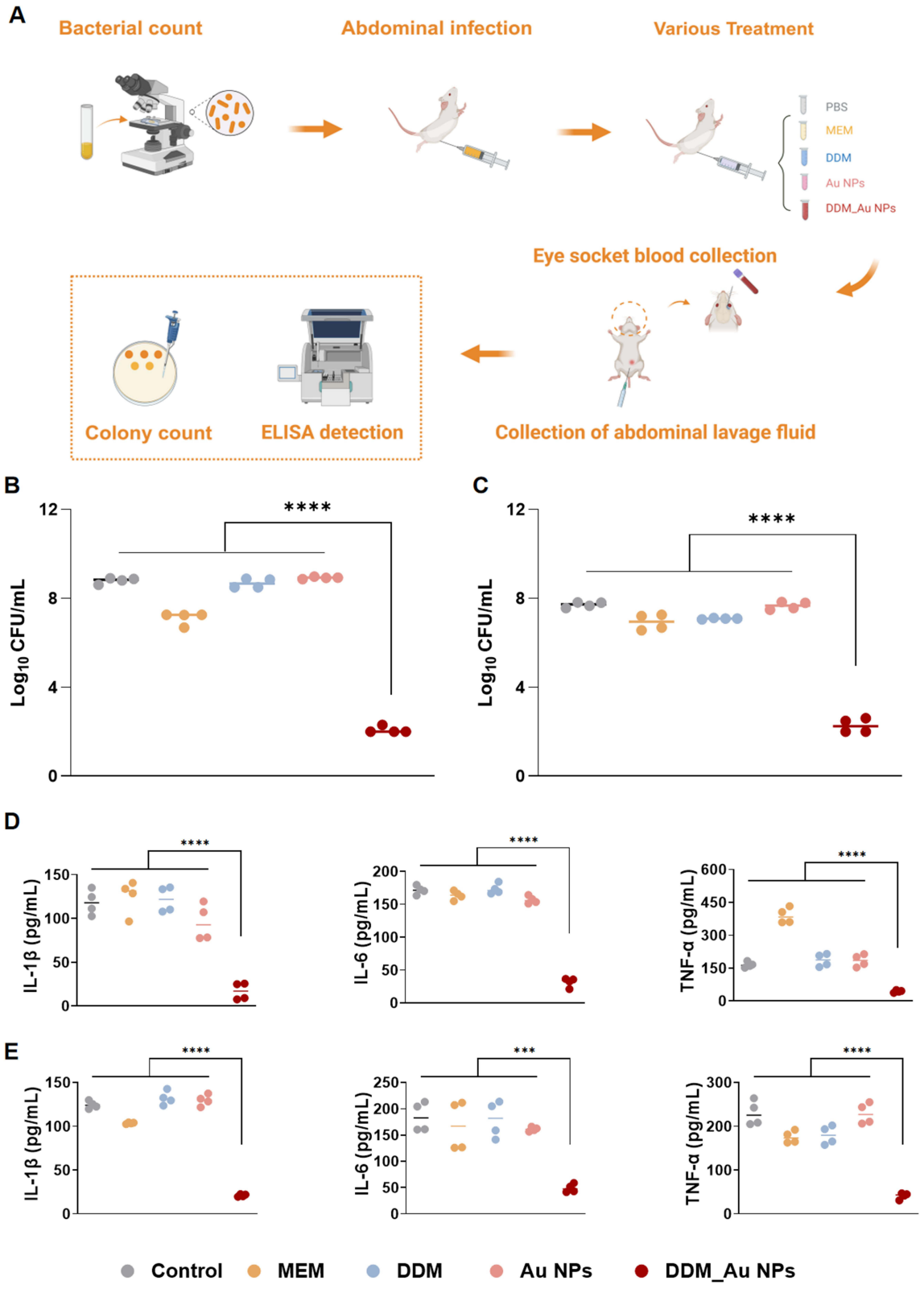

Figure 10 Mouse intraperitoneal infection model. (**A**) Depiction of the experimental process; (**B**) Bacterial count in the peritoneal lavage fluid of mice; (**C**) Bacterial count in the blood of mice; (**D**) The expression of inflammatory factors in mouse peritoneal lavage fluid; (**E**) The expression of inflammatory factors in the blood of mice; ****$p <$ 0.0001. Data are presented as the mean ±SD (n = 4).

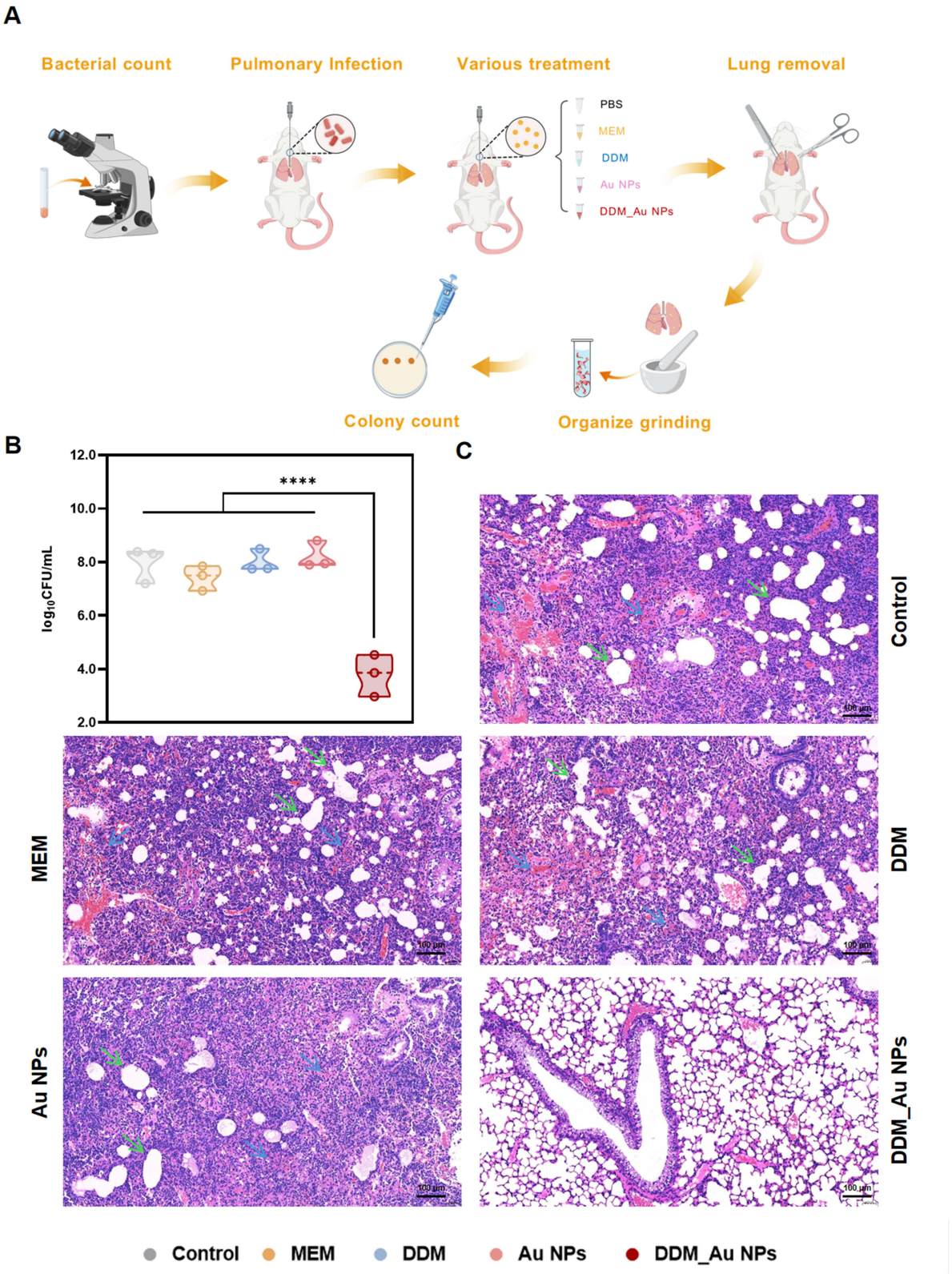

Figure 11 Mouse lung infection model. (**A**) Graphical representation of the experimental process, created using BioGDP.com; (**B**) Bacterial counts of the murine lung tissues; (**C**) Sections of mouse lungs of H&E Staining (200x magnification). Blue arrows: dispersed red blood cells, green arrows: compensatory expanded alveoli; ****$P < 0.0001$. Data are presented as the mean ±SD (n = 3).

https://doi.org/10.2147/IJN.S532807

based antimicrobial products include silver nanoparticle formulations (eg, Silvadene®) and liposomal drug delivery systems (eg, AmBisome®), which are widely used in treating wound infections.[57] By contrast, while Au NPs have not yet received FDA approval for systemic antimicrobial use, they are approved for medical imaging and cancer treatment, such as in AuroShell® Au NPs used for photothermal therapy (PTT).[58] These examples underscore the excellent biocompatibility and clinical potential of Au NPs, reinforcing confidence in the development of DDM-functionalized Au NP-based antimicrobials. Our findings offer a novel direction for creating clinically viable therapeutic agents against CRE infections. Nonetheless, further refinement of the nanosynthesis protocol is required to generate more uniform and stable antiparasitic drug-based Au NPs suitable for clinical application. We propose that other antiparasitic drugs with multiple reducing groups may also serve as effective nanogold functionalizing agents, and further experimental validation is currently underway.

The antibacterial mechanisms of Au NPs are largely influenced by the nature of their surface modifications. Most drug-functionalized Au NPs, including the DDM_Au NPs explored in this study, markedly increase intracellular ROS production.[15,18] However, excessive ROS accumulation may also induce cytotoxic effects in host tissues.[59] Both thymol- and DDM-coated Au NPs have been shown to compromise bacterial membrane integrity, likely by exerting mechanical stress.[19] Au NPs with diameters exceeding 10 nm tend to adhere to bacterial membranes, increase membrane tension, and provoke physical damage, ultimately leading to membrane rupture and bacterial death.[60] In the case of DDM_Au NPs, the DDM moiety appears to facilitate membrane destabilization, aligning with previous studies that demonstrated DDM's disruptive effects on bacterial membranes.[21] Eugenol-conjugated Au NPs have been reported to prevent *Pseudomonas aeruginosa* biofilm development by suppressing quorum-sensing gene expression.[25] Likewise, DDM_Au NPs inhibited the transcription of biofilm-related genes in CRE. In a related study, Zhang et al showed that Au NPs functionalized with 5-amino-2-mercaptobenzimidazole disrupted intracellular oxidative balance and suppressed succinate synthesis in bacteria.[37]

Among hospital-acquired infections, catheter-associated urinary tract infections are particularly common in patients undergoing prolonged mechanical ventilation, urinary catheterization, or intravenous line maintenance, placing them at heightened risk of CRE colonization and infection.[61] CRE is frequently isolated from urine samples and is implicated in persistent bacteriuria, complicated urinary tract infections, and bloodstream infections, all of which can result in severe or fatal outcomes. A retrospective study reported a 54% mortality rate in cases of bacteremia caused by carbapenem-resistant *K. pneumoniae*.[62] In this study, DDM_Au NPs demonstrated strong antibiofilm activity against CRE, particularly in eliminating biofilms on urinary catheter surfaces. Notably, these nanoparticles achieved a >6 $\log_{10}$ reduction in viable bacterial counts within catheter-associated biofilms of carbapenem-resistant *E. coli*. To the best of our knowledge, such potent antibiofilm effects by antiparasitic drug-functionalized Au NPs against CRE have not been previously reported. These findings highlight the potential of DDM_Au NPs in clinical applications, including catheter surface modification or as disinfectant additives in catheter-immersion protocols.[63]

In summary, AMR remains an urgent and evolving global health threat. The development of nanoscale antimicrobial platforms, such as DDM_Au NPs, complements global strategies like the World Health Organization's Global Action Plan on AMR.[64] Currently, the clinical approval of nanomedicines is regulated by the FDA, typically through frameworks used for small-molecule drugs, biologics, or medical devices.[65] Moving forward, efforts should focus on optimizing the synthesis of DDM_Au NPs to enhance their colloidal stability, dispersibility, and batch-to-batch consistency. Rigorous evaluation of their formulation properties, long-term biocompatibility, pharmacokinetics, biodistribution, and therapeutic performance in vivo will be essential for translational advancement.

Conclusions

Amid the mounting global crisis of antibiotic resistance—particularly from CRE—repurposing clinically approved drugs via nanomaterial-based delivery systems offers a promising therapeutic paradigm. In this work, we present the facile, one-pot synthesis of Au NPs functionalized with the antiparasitic agent DDM, referred to as DDM_Au NPs. This nanoformulation substantially augments the intrinsic antimicrobial and antibiofilm activity of DDM. The DDM_Au NPs demonstrated robust, multi-modal activity against CRE, eliciting potent bactericidal and anti-inflammatory effects in murine models of abdominal and pulmonary infections. These findings underscore the potential of DDM_Au NPs as

a next-generation therapeutic platform for combating CRE-associated diseases. Furthermore, the nanoformulation efficiently disrupted biofilms formed on contaminated urinary catheters, emphasizing its clinical applicability in preventing device-associated nosocomial infections. Importantly, in vivo assessments revealed that DDM_Au NPs possess a favorable biosafety profile, strengthening their candidacy for translational development. Collectively, this study not only introduces a novel nanotherapeutic approach for CRE treatment but also advocates for broader exploration of antiparasitic drug-functionalized nanomaterials as a strategic avenue for targeting a spectrum of multidrug-resistant pathogens, paving the way for future clinical translation.

Data Sharing Statement

The data used during the current study are available from the corresponding author (Dr. Tieli Zhou) upon a reasonable request.

Ethics Approval and Consent to Participate

The use of bacterial isolates for research purposes was approved by the Ethics Committee for Clinical Research of the First Affiliated Hospital of Wenzhou Medical University (Approval No. KY2025-R150). Considering the retrospective design of the study, the requirement for informed consent was waived. All animal experiments were approved by the Ethics Committee of the First Affiliated Hospital of Wenzhou Medical University (Approval No. SYXK 2021-0017) and conducted in accordance with the Wenzhou Laboratory Animal Welfare and Ethics Guidelines. This study complies with the Declaration of Helsinki and its latest amendments.

Acknowledgments

The authors extend their appreciation to the Scientific Research Center of Wenzhou Medical University for providing consultation and access to instruments.

Funding

This work was funded by the Key Laboratory of Clinical Laboratory Diagnosis and Translational Research of Zhejiang Province (2022E10022).

Disclosure

The authors declare no competing interests in this work.

References

1. Murray CJL, Ikuta KS, Sharara F. Global burden of bacterial antimicrobial resistance in 2019: a systematic analysis. *Lancet*. 2022;399 (10325):629–655. doi:10.1016/S0140-6736(21)02724-0
2. World Health Organization. WHO updates list of drug-resistant bacteria most threatening to human health 2025. Available from: https://www.who.int/news/item/17-05-2024-who-updates-list-of-drug-resistant-bacteria-most-threatening-to-human-health. Accessed August 15, 2025.
3. Aiesh BM, Maali Y, Qandeel F, et al. Epidemiology and clinical characteristics of patients with carbapenem-resistant enterobacterales infections: experience from a large tertiary care center in a developing country. *BMC Infect Dis*. 2023;23:644. doi:10.1186/s12879-023-08643-9
4. Martin A, Fahrbach K, Zhao Q, Lodise T. Association between carbapenem resistance and mortality among adult, hospitalized patients with serious infections due to enterobacteriaceae: results of a systematic literature review and meta-analysis. *Open Forum Infect Dis*. 2018;5:ofy150. doi:10.1093/ofid/ofy150
5. Coates ARM, Hu Y, Holt J, Yeh P. Antibiotic combination therapy against resistant bacterial infections: synergy, rejuvenation and resistance reduction. *Expert Rev Anti Infect Ther*. 2020;18:5–15. doi:10.1080/14787210.2020.1705155
6. Mousavi SM, Hashemi SA, Ghasemi Y, et al. Green synthesis of silver nanoparticles toward bio and medical applications: review study. *Artif Cells Nanomed Biotechnol*. 2018;46:S855–s872. doi:10.1080/21691401.2018.1517769
7. Frei A, Verderosa AD, Elliott AG, Zuegg J, Blaskovich MAT. Metals to combat antimicrobial resistance. *Nat Rev Chem*. 2023;7:202–224. doi:10.1038/s41570-023-00463-4
8. Okkeh M, Bloise N, Restivo E, et al. Gold nanoparticles: can they be the next magic bullet for multidrug-resistant bacteria? *Nanomaterials*. 2021;11:312. doi:10.3390/nano11020312
9. Hernández-Sierra JF, Ruiz F, Pena DC, et al. The antimicrobial sensitivity of Streptococcus mutans to nanoparticles of silver, zinc oxide, and gold. *Nanomedicine*. 2008;4:237–240. doi:10.1016/j.nano.2008.04.005
10. Zhang N, Xiong G, Liu Z. Toxicity of metal-based nanoparticles: challenges in the nano era. *Front Bioeng Biotechnol*. 2022;10:1001572. doi:10.3389/fbioe.2022.1001572

11. Muhaimin M, Chaerunisaa AY, Dewi MK, Khatib A, Hazrina A. The toxicological profile of active pharmaceutical ingredients-containing nanoparticles: classification, mechanistic pathways, and health implications. *Pharmaceuticals*. 2025;18:703. doi:10.3390/ph18050703
12. Singh S, Vidyarthi AS, Nigam VK, Dev A. Extracellular facile biosynthesis, characterization and stability of gold nanoparticles by Bacillus licheniformis. *Artif Cells Nanomed Biotechnol*. 2014;42:6–12. doi:10.3109/21691401.2012.759122
13. Wahab S, Salman A, Khan Z, et al. Metallic nanoparticles: a promising arsenal against antimicrobial resistance-unraveling mechanisms and enhancing medication efficacy. *Int J Mol Sci*. 2023;24(19):14897. doi:10.3390/ijms241914897
14. Wang L, Zheng W, Li S, Zhong L, Jiang X. Aminophenol-decorated gold nanoparticles for curing bacterial infections. *Nano Lett*. 2022;22:3576–3582. doi:10.1021/acs.nanolett.1c04968
15. Huang Z, Liu H, Zhang X, et al. Ceftazidime-decorated gold nanoparticles: a promising strategy against clinical ceftazidime-avibactam-resistant Enterobacteriaceae with different resistance mechanisms. *Antimicrob Agents Chemother*. 2023;67:e0026223. doi:10.1128/aac.00262-23
16. Hutchinson N, Wu Y, Wang Y, et al. Green synthesis of gold nanoparticles using upland cress and their biochemical characterization and assessment. *Nanomaterials*. 2021;12(1):12. doi:10.3390/nano12010012
17. Peng H, Borg RE, Dow LP, Pruitt BL, Chen IA. Controlled phage therapy by photothermal ablation of specific bacterial species using gold nanorods targeted by chimeric phages. *Proc Natl Acad Sci U S A*. 2020;117:1951–1961. doi:10.1073/pnas.1913234117
18. Liu H, Huang Z, Chen H, et al. A potential strategy against clinical carbapenem-resistant Enterobacteriaceae: antimicrobial activity study of sweetener-decorated gold nanoparticles in vitro and in vivo. *J Nanobiotechnology*. 2023;21:409. doi:10.1186/s12951-023-02149-x
19. Huang Z, Zhang X, Yao Z, et al. Thymol-decorated gold nanoparticles for curing clinical infections caused by bacteria resistant to last-resort antibiotics. *mSphere*. 2023;8:e0054922. doi:10.1128/msphere.00549-22
20. Guo W, Liu Y, Yao Z, et al. Bithionol restores sensitivity of multidrug-resistant gram-negative bacteria to colistin with antimicrobial and anti-biofilm effects. *ACS Infect Dis*. 2023;9:1634–1646. doi:10.1021/acsinfecdis.3c00257
21. Amakawa M, Gunawardana S, Jabbour A, et al. Repurposing clinically approved drugs for the treatment of Bacillus cereus, a surrogate for Bacillus anthracis. *ACS Omega*. 2020;5:21929–21939. doi:10.1021/acsomega.0c03207
22. Khaw TH, Wong SNM, Herle G, et al. Identification of bithionol, dichlorophen, and miconazole as antibacterial agents against acinetobacter calcoaceticus. *ACS Omega*. 2020;5:23951–23959. doi:10.1021/acsomega.0c03211
23. Yamarik TA. Safety assessment of dichlorophene and chlorophene. *Int J Toxicol*. 2004;23(Suppl 1):1–27.
24. Singh R, Patil S, Singh N, Gupta S. Dual functionality nanobioconjugates targeting intracellular bacteria in cancer cells with enhanced antimicrobial activity. *Sci Rep*. 2017;7:5792. doi:10.1038/s41598-017-06014-4
25. Chen H, Hu P, Wang Y, et al. From quorum sensing inhibition to antimicrobial defense: the dual role of eugenol-gold nanoparticles against carbapenem-resistant Pseudomonas aeruginosa. *Colloids Surf B Biointerfaces*. 2025;247:114415. doi:10.1016/j.colsurfb.2024.114415
26. Yao Z, Feng L, Zhao Y, et al. Thymol increases sensitivity of clinical Col-R gram-negative bacteria to colistin. *Microbiol Spectr*. 2022;10:e0018422. doi:10.1128/spectrum.00184-22
27. Darwish RM, Salama AH, Mugoša S. Study the effect of conjugate novel ultra-short antimicrobial peptide with silver nanoparticles against methicillin resistant S. aureus and ESBL E. coli. *Antibiotics*. 2022;12(1):11. doi:10.3390/antibiotics12010011
28. Gut AM, Vasiljevic T, Yeager T, Donkor ON. Anti-salmonella properties of kefir yeast isolates: an in vitro screening for potential infection control. *Saudi J Biol Sci*. 2022;29:550–563. doi:10.1016/j.sjbs.2021.09.025
29. Ye Z, Ye L, Li D, et al. Effects of daphnetin on biofilm formation and motility of pseudomonas aeruginosa. *Front Cell Infect Microbiol*. 2022;12:1033540. doi:10.3389/fcimb.2022.1033540
30. Ravikumar V, Mijakovic I, Pandit S. Antimicrobial activity of graphene oxide contributes to alteration of key stress-related and membrane bound proteins. *Int J Nanomedicine*. 2022;17:6707–6721.
31. Navarro S, Sherman E, Colmer-Hamood JA, et al. Urinary catheters coated with a novel biofilm preventative agent inhibit biofilm development by diverse bacterial uropathogens. *Antibiotics*. 2022;12(1):11.
32. Byun KH, Han SH, Choi MW, Kim BH, Ha SD. Efficacy of disinfectant and bacteriophage mixture against planktonic and biofilm state of Listeria monocytogenes to control in the food industry. *Int J Food Microbiol*. 2024;413:110587. doi:10.1016/j.ijfoodmicro.2024.110587
33. Elken EM, Tan ZN, Wang Q, et al. Impact of Sub-MIC eugenol on Klebsiella pneumoniae biofilm formation via upregulation of rcsB. *Front Vet Sci*. 2022;9:945491. doi:10.3389/fvets.2022.945491
34. Huang LL, Tang M, Du QQ, et al. The effects and mechanisms of a biosynthetic ginsenoside 3β,12β-Di-O-Glc-PPD on non-small cell lung cancer. *Onco Targets Ther*. 2019;12:7375–7385.
35. Olsowski M, Hoffmann F, Hain A, et al. Exophiala dermatitidis isolates from various sources: using alternative invertebrate host organisms (Caenorhabditis elegans and Galleria mellonella) to determine virulence. *Sci Rep*. 2018;8:12747. doi:10.1038/s41598-018-30909-5
36. Asai M, Li Y, Newton SM, Robertson BD, Langford PR. Galleria mellonella-intracellular bacteria pathogen infection models: the ins and outs. *FEMS Microbiol Rev*. 2023;47.
37. Zhang J, Zhang X, Yao Z, et al. Gold nanoparticles functionalized with 5-amino-2-mercaptobenzimidazole: a promising antimicrobial strategy against carbapenem-resistant gram-negative bacteria. *Int J Nanomedicine*. 2025;20:2485–2504. doi:10.2147/IJN.S502139
38. Fan T, Guo W, Shao T, et al. Design, synthesis and evaluation of phenylthiazole and phenylthiophene pyrimidindiamine derivatives targeting the bacterial membrane. *Eur J Med Chem*. 2020;190:112141. doi:10.1016/j.ejmech.2020.112141
39. Hu JJ, Lin YS, Zhang JC, Wang YH. Vitamin D improves Klebsiella-induced severe pneumonia in rats by regulating intestinal microbiota. *Infect Drug Resist*. 2024;17:475–484. doi:10.2147/IDR.S442330
40. Pathania D, Sharma M, Thakur P, et al. Exploring phytochemical composition, photocatalytic, antibacterial, and antifungal efficacies of Au NPs supported by Cymbopogon flexuosus essential oil. *Sci Rep*. 2022;12:14249. doi:10.1038/s41598-022-15899-9
41. Zeng W, Liao W, Zhao Y, et al. A selective medium for screening ceftazidime/avibactam resistance in carbapenem-resistant Enterobacterales. *Front Microbiol*. 2022;13:956044. doi:10.3389/fmicb.2022.956044
42. Feng L, Zhao Y, Yao Z, et al. Rapid ResaCeftazidime-Avibactam Enterobacterales NP test: rapid detection of Ceftazidime-avibactam susceptibility in Enterobacterales. *J Clin Microbiol*. 2022;60:e0000422. doi:10.1128/jcm.00004-22
43. Lin Q, Wang Y, Yu J, et al. Bacterial characteristics of carbapenem-resistant Enterobacteriaceae (CRE) colonized strains and their correlation with subsequent infection. *BMC Infect Dis*. 2021;21:638. doi:10.1186/s12879-021-06315-0

44. Gollan B, Grabe G, Michaux C, Helaine S. Bacterial Persisters and Infection: past, Present, and progressing. *Annu Rev Microbiol*. 2019;73:359–385. doi:10.1146/annurev-micro-020518-115650
45. Zhang Z, Chen J, Zou L, et al. Preparation, characterization, and Staphylococcus aureus biofilm elimination effect of baicalein-loaded β-cyclodextrin-grafted chitosan nanoparticles. *Int J Nanomedicine*. 2022;17:5287–5302. doi:10.2147/IJN.S383182
46. Wassmann CS, Højrup P, Klitgaard JK. Cannabidiol is an effective helper compound in combination with bacitracin to kill Gram-positive bacteria. *Sci Rep*. 2020;10:4112. doi:10.1038/s41598-020-60952-0
47. Di Petrillo A, Orrù G, Fais A, Fantini MC. Quercetin and its derivates as antiviral potentials: a comprehensive review. *Phytother Res*. 2022;36:266–278. doi:10.1002/ptr.7309
48. Ciofu O, Moser C, Jensen P, Høiby N. Tolerance and resistance of microbial biofilms. *Nat Rev Microbiol*. 2022;20(10):621–635. doi:10.1038/s41579-022-00682-4
49. Bai Y, Wang W, Shi M, et al. Novel antibiofilm inhibitor ginkgetin as an antibacterial synergist against Escherichia coli. *Int J Mol Sci*. 2022;24:23. doi:10.3390/ijms24010023
50. Piatek M, Sheehan G, Kavanagh K. UtilisingGalleria mellonella larvae for studying in vivo activity of conventional and novel antimicrobial agents. *Pathog Dis*. 2020;78. doi:10.1093/femspd/ftaa059
51. Naghavi M, Vollset SE, Ikuta KS. Global burden of bacterial antimicrobial resistance 1990–2021: a systematic analysis with forecasts to 2050. *Lancet*. 2024;404:1199–1226. doi:10.1016/S0140-6736(24)01867-1
52. Nordmann P, Poirel L. Epidemiology and diagnostics of carbapenem resistance in gram-negative bacteria. *Clin Infect Dis*. 2019;69:S521–s528. doi:10.1093/cid/ciz824
53. Sabino S, Soares S, Ramos F, et al. A cohort study of the impact of carbapenem-resistant Enterobacteriaceae infections on mortality of patients presenting with sepsis. *mSphere*. 2019;4. doi:10.1128/mSphere.00052-19
54. Zhao G, Zheng J, Wu J, et al. Mechanistic understanding of differences in cytotoxicity induced by food additives methyleugenol and methylisoeugenol. *J Agric Food Chem*. 2025;73:3154–3169. doi:10.1021/acs.jafc.4c12910
55. Fogel MN, Khalil A, Khaled SF, et al. Aspartame and its potential neurocognitive effects in humans. *Nutr Rev*. 2025. doi:10.1093/nutrit/nuaf103
56. Rousar T, Handl J, Capek J, et al. Cysteine conjugates of Acetaminophen and p-aminophenol are potent inducers of cellular impairment in human proximal tubular kidney HK-2 cells. *Arch Toxicol*. 2023;97:2943–2954. doi:10.1007/s00204-023-03569-2
57. Aflakian F, Mirzavi F, Aiyelabegan HT, et al. Nanoparticles-based therapeutics for the management of bacterial infections: a special emphasis on FDA approved products and clinical trials. *Eur J Pharm Sci*. 2023;188:106515. doi:10.1016/j.ejps.2023.106515
58. Sibuyi NRS, Moabelo KL, Fadaka AO, et al. Multifunctional gold nanoparticles for improved diagnostic and therapeutic applications: a review. *Nanoscale Res Lett*. 2021;16:174. doi:10.1186/s11671-021-03632-w
59. Cui Y, Zhao Y, Tian Y, et al. The molecular mechanism of action of bactericidal gold nanoparticles on Escherichia coli. *Biomaterials*. 2012;33(7):2327–2333. doi:10.1016/j.biomaterials.2011.11.057
60. Linklater DP, Baulin VA, Le Guével X, et al. Antibacterial action of nanoparticles by lethal stretching of bacterial cell membranes. *Adv Mater*. 2020;32:e2005679. doi:10.1002/adma.202005679
61. Ukuhor HO. The interrelationships between antimicrobial resistance, COVID-19, past, and future pandemics. *J Infect Public Health*. 2021;14:53–60. doi:10.1016/j.jiph.2020.10.018
62. Xu L, Sun X, Ma X. Systematic review and meta-analysis of mortality of patients infected with carbapenem-resistant Klebsiella pneumoniae. *Ann Clin Microbiol Antimicrob*. 2017;16:18. doi:10.1186/s12941-017-0191-3
63. Geyer F, D'Acunzi M, Yang CY, et al. How to coat the inside of narrow and long tubes with a super-liquid-repellent layer-a promising candidate for antibacterial catheters. *Adv Mater*. 2019;31:e1801324. doi:10.1002/adma.201801324
64. Iwu CD, Patrick SM. An insight into the implementation of the global action plan on antimicrobial resistance in the WHO African region: a roadmap for action. *Int J Antimicrob Agents*. 2021;58:106411. doi:10.1016/j.ijantimicag.2021.106411
65. Bobo D, Robinson KJ, Islam J, Thurecht KJ, Corrie SR. Nanoparticle-based medicines: a review of FDA-approved materials and clinical trials to date. *Pharm Res*. 2016;33:2373–2387. doi:10.1007/s11095-016-1958-5